

Return of the features

Efficient feature selection and interpretation for photometric redshifts

A. D’Isanto¹, S. Cavuoti^{2,3,4}, F. Gieseke⁵, and K.L. Polsterer¹

¹ Astrominformatics group, Heidelberg Institute for Theoretical Studies, Schloss-Wolfsbrunnenweg 35, 69118 Heidelberg, Germany
e-mail: antonio.disanto@h-its.org, e-mail: kai.polsterer@h-its.org

² Department of Physics “E. Pancini”, University Federico II, via Cinthia 6, I-80126, Napoli, Italy

³ INAF - Astronomical Observatory of Capodimonte, via Moiariello 16, 80131 Napoli, Italy

⁴ INFN - Section of Naples, via Cinthia 9, 80126 Napoli, Italy e-mail: stefano.cavuoti@gmail.com

⁵ Machine Learning Group Image Section, Department of Computer Science, University of Copenhagen, Sigurdsgade 41, 2200 København N, Denmark

Received

ABSTRACT

Context. The explosion of data in the recent years generated an increasing need of new analysis techniques in order to extract knowledge from massive data-sets. Machine learning proved particularly useful to perform this task. Fully automatized methods (e.g. deep neural networks) have recently gathered great popularity, even though those methods are often lacking physical interpretability. In contrast, feature based approaches can provide both, well performing models as well as understandable causalities with respect to the found correlations between features and physical processes.

Aims. Efficient feature selection is an essential tool to boost the performance of machine learning models. In this work, we propose a forward selection method in order to compute, evaluate and characterize better performing features for regression and classification problems. Given the importance of photometric redshift estimation, we adopt it as our use case.

Methods. We synthetically created 4,520 features, by combining magnitudes, errors, radii and ellipticities of quasars, taken from the SDSS. We apply a forward selection process, a recursive method in which a huge number of feature sets is tested through a k-Nearest-Neighbors algorithm, leading to a tree of feature sets. The branches of the feature tree are then used to perform experiments with the random forest, in order to validate the best set with an alternative model.

Results. We demonstrate that the sets of features determined with our approach improve the performances of the regression models significantly when compared to the performance of the classic features from the literature. The found features are unexpected and surprising, being very different from the classic features. Therefore, a method to interpret some of the found features in a physical context is presented.

Conclusions. The feature selection methodology described here is very general and can be used to improve the performance of machine learning models for any regression or classification task.

Key words. Astronomical instrumentation, methods and techniques – Methods: data analysis – Methods: statistical – Galaxies: distances and redshifts – quasars: general

1. Introduction

In the recent years, astronomy has experienced a true explosion in the amount and complexity of the available data. The new generation of digital surveys is opening a new era for the astronomical research, characterized by the necessity to analyze data-sets falling into the Tera-scale and Peta-scale regime. This is leading to the necessity of a completely different approach with respect to the process of knowledge discovery. In fact, the main challenge will no longer be obtaining data in order to prove or disprove a certain hypothesis, but rather to mine into the data in order to find interesting trends and unknown patterns. The process of discovery will not be driven by new kinds of instrumentation to explore yet unobserved regimes but by efficient combination and analysis of already existing measurements. Such an approach requires the development of new techniques and tools in order to deal with this explosion of data, that are far beyond any possibility of a manual inspection by humans. This necessity will become urgent in the next years, when surveys like the Large Synoptic Survey Telescope (LSST Ivezić et al. 2008), the Square

Kilometer Array (SKA Taylor 2008), and many others, will become available. Therefore, machine learning techniques are becoming a necessity, in order to automatize the process of knowledge extraction from big data-sets. In the last decade, machine learning has proved to be particularly useful to solve astrophysical complex non-linear problems, both for regression (see for instance Hildebrandt et al. 2010; Bilicki et al. 2014; Cavuoti et al. 2015; Hoyle 2016; Beck et al. 2017) and classification tasks (see Mahabal et al. 2008; Rimoldini et al. 2012; Cavuoti et al. 2013a; D’Isanto et al. 2016; Smirnov & Markov 2017; Benavente et al. 2017). These techniques find nowadays many applications in almost all the fields of science and not only (Hey et al. 2009). In the literature, two main machine learning branches can be found that deal with the selection of the most relevant information contained in the data. The first *traditional* way consists in the extraction and selection of manually crafted features which are theoretically more suitable to optimize the performance. In Donalek et al. (2013) feature selection strategies are compared in an astrophysical context.

The second option is using automatic feature selection models and became more popular in the last years. E.g. Athiwaratkun & Kang (2015) delegate this task to the machine by analyzing the automatically extracted feature representations of convolutional neural networks. In convolutional neural networks, during the training phase the model itself determines and optimizes the extraction of available information in order to obtain the best performance. The challenge of feature selection is fundamental for machine learning applications, due to the necessity to balance between overfitting and the curse of dimensionality (Bishop 2006), which arises when dealing with very high-dimensional spaces. Therefore a clever process of feature selection is needed to overcome this issue. In this setting, a different strategy was chosen for this work, in which a forward selection algorithm (Guyon & Elisseeff 2003) is adopted to identify the best performing ones out of thousands of features. We decided to apply this procedure in a very important field: photometric redshift estimation. Due to the enormous importance that this measure has in cosmology, great efforts have been lavished by the astronomical community to build efficient methods for the determination of affordable and precise photometric redshifts (Richards et al. 2001; Hildebrandt et al. 2008; Ball et al. 2008; Hildebrandt et al. 2010). Photometric redshifts are of extreme importance with respect to upcoming missions, e.g. the soon-coming Euclid mission (Laureijs et al. 2011), which will be based on the availability of photometric redshift measures, and the Kilo Degree Survey (KiDS de Jong et al. 2017) which aims to map the large-scale matter distribution in the Universe, using weak lensing shear and photometric redshift measurements (Hildebrandt et al. 2016; Tortora et al. 2016; Harnois-Déraps et al. 2017; Joudaki et al. 2017; Köhlinger et al. 2017). Furthermore, photometric redshifts estimation is crucial for several other projects, the most important being EMU (Norris et al. 2011), LOFAR (van Haarlem et al. 2013), Dark Energy Survey (Bonnett et al. 2016), PANSTARRS (Chambers et al. 2016) and VST-VOICE (Vaccari et al. 2016). In this sense, we propose to invert the task of photometric redshift estimation. That is to say, stated the possibility to determine the redshift of a galaxy based on its photometry, we want to build a method which allows to investigate the parameter space and to extract the features to be used to achieve the best performance. As deeply analyzed in D’Isanto & Polsterer (2018), the implementation of deep learning techniques is providing an alternative to feature-based methods, allowing the estimation of photometric redshifts directly from images. The main concerns when adopting deep learning models are related to the amount of data needed to efficiently perform the training of the networks, the cost in term of resources and computation time and the lack of interpretability related to the features automatically extracted. In fact, deep learning models can easily become like magic boxes and it is really hard to assign any kind of physical meaning to the features estimated by the model itself. Therefore, a catalog-based approach still has great importance, due to the gain in time, resources and interpretability. In particular, this is true if a set of significant features is provided, in order to concentrate the important information with respect to the problem in a reduced number of parameters. Both methods, based on automatically extracted features or on selected features constitute the starting point to build an efficient and performing model for redshift estimation, respectively. The topic of feature selection is a well treated subject in literature (see for example Rimoldini et al. 2012; Tangaro et al. 2015; Hoyle et al. 2015; D’Isanto et al. 2016). The used forward selection approach we used (Gieseke et al. 2014) is meant to select between thousands

of features generated by combining plain photometric features as they are given in the original catalog. No matter what selection strategy is applied, the final results have to be compared to those obtained with the traditional features from the literature (D’Abrusco et al. 2007; Richards et al. 2009; Laurino et al. 2011) and with automatically extracted features. The aim is to find the subsets which give a better performance for the proposed experiments, mining into this new, huge feature space and to build a method useful to find the best features for any kind of problem. Moreover, we propose to analyze the obtained features, in order to give them a physical explanation and a connection with the processes occurring in the specific category of sources. Such an approach also demands a huge effort in terms of computational time and resources. Therefore, we need an extreme parallelization to deal with this task. This has been done through the intensive use of graphics processing units (GPU), a technology which is opening new doors for the Astrominformatics (Cavuoti et al. 2013b; Polsterer et al. 2015; D’Isanto & Polsterer 2018), allowing the adoption of deep learning and/or massive feature selection strategies. In particular, in this work, the feature combinations are computed following Gieseke et al. (2014) and Polsterer et al. (2014), using a GPU cluster equipped with four Nvidia Pascal P40 graphic cards¹. Likewise to Zhang et al. (2013), k-Nearest-Neighbors (kNN Fix & Hodges 1951) model is used, running recursive experiments in order to estimate the best features through the forward selection process. This choice has been done because the kNN model scales very well with the use of GPU, with respect to performance and quality of the prediction, as shown in Heineremann et al. (2013). In this way, for each run of the experiment, the most contributing features are identified and added to previous subsets. Thereby, a tree of feature groups is created which afterwards can be compared with the traditional ones. The validation experiments are performed using a random forest (RF) model (Carliles et al. 2010, application in astronomy). We will show that this approach can strongly improve the performance for the task of redshift estimation. The improvement is due to the identification of specific feature subsets containing more information and capable to better characterize the physics of the sources. In the present work, we perform the experiments on quasar data samples extracted from the Sloan Digital Sky Survey Data Release 7 (SDSS DR7 Abazajian et al. 2009) and Data Release 9 (SDSS DR9 Ahn et al. 2012). The proposed approach is very general and could be also used to solve many other tasks in astronomy, including both, regression and classification problems.

Outline: In Sec. 2 the methodology and models used to perform the experiments are described together with the statistical estimators used to evaluate the performance. The strategy adopted for the feature selection is also explained. Sec. 3 is dedicated to the data used and the feature extraction process. In Sec. 4 the experiments performed and the results obtained are described. Finally, in Sec. 5 the results are discussed in detail and in Sec. 6 some conclusions are drawn.

2. Methods

The main purpose of this work is to build an efficient method capable to generate, handle and select the best features for photometric redshift estimation, even though the proposed method is able to deal also with any other task of regression or even classification. We calculate thousands of feature combinations of photometric data taken from quasars. Then, a forward selection

¹ <https://images.nvidia.com/content/pdf/tesla/184427-Tesla-P40>

process is applied, as it will be explained in more detail in the next sections. This is done to build a *tree* of best performing feature subsets. This method has to be considered as an alternative to the automatic features extraction used in D’Isanto & Polsterer (2018). Both methods can be useful and efficient, depending on the nature of the problem, on the availability of data and resources. For this reason, the results obtained with both methods will be compared. The experimental strategy is based on the application of two different machine learning models and evaluated on the basis of several statistical tools. In the following these models, i.e. kNN and RF, are presented. The strategy used to perform the feature selection is then depicted in detail and a description of the statistical framework used for the experiments evaluation and of the cross validation algorithm is given.

2.1. Regression models

As aforementioned our method makes use of kNN and RF models which are described in detail in the following subsections, while the details regarding the Deep Convolutional Mixture Density Network (DCMDN) used to compare the results with an automatic features extraction based model can be found in D’Isanto & Polsterer (2018).

2.1.1. kNN

The kNN (Fix & Hodges 1951) is a machine learning model used both for regression and classification tasks (Zhang et al. 2013). This model explores the feature space by estimating the k nearest points (or neighbors) belonging to the training sample with respect to each test item. In our case the distance involved is calculated through a Euclidean metric. In the case of a regression problem (like redshift estimation) the kNN algorithm is used to find a continuous variable averaging the distances of the k selected neighbors. The efficiency of the algorithm is strongly related to the choice of the parameter k , which represents the number of neighbors to be selected from the training set. The best choice of this parameter is directly related to the input data, their complexity and the way in which the input space is sampled. Clearly, the most simple case is a model with $k = 1$. In this case, a prediction equal to the target of the closest pattern in the training set is associated to each pattern. Increasing the k parameter could improve the precision of the model (this is due to the increasing generalization capability), but can also generate overfitting (Duda et al. 2000). In our experiments, the choice of the k parameter was part of the learning task by evaluating a set of possible values. The kNN is one of the simplest machine learning algorithms, but even if it could be outperformed by more complex models, it has the advantage of being very fast and in any case quite efficient. Another possible problem concerning the use of the kNN model is given by possible differences in the range of the input features. This could generate problems and misleading results in the estimation of distances in the parameter space. For this reason, all the features used in this work have been normalized using the min-max normalization technique (Aksoy & Haralick 2000).

2.1.2. Random Forest

The RF (Breiman et al. 1984) is one of the most popular ensemble based machine learning models, and could be used for regression and classification tasks (see Carliles et al. 2010, for an application to photometric redshift estimation). It is an ensemble

of decision trees, where each tree is meant to partition the feature space in order to find the best split that minimizes the variance. Each decision tree is built by adding leaf nodes where the input data are partitioned with respect to a different chosen feature, repeating the process for all the possible choices of variables to be split. In case of a regression problem, the root mean square error (RMSE) is computed for each possible partition, and the partition which minimizes the RMSE is chosen. The RF averages the results provided by many decision trees, each trained on a different part of the training set through the bagging technique (Breiman 1996). This avoids overfitting due to single decision trees growing too deep. Moreover, the decision tree makes use of the bootstrapping technique (Breiman 1996), in order to increase performance and stability of the method and reduce overfitting at the same time. This consists in giving, as input, to each decision tree a different random sub-sample of the training data. The RF uses the feature bagging during the training phase. This consists in selecting a random subset of features at each split. Bootstrapping and bagging help avoiding correlations between single decision trees, that could appear when training them on the same training set and in the presence of strong features selected multiple times.

2.2. Features selection strategy

The huge number of features evaluated, as described in Sec. 3, imposes the necessity to establish an efficient feature selection process. In fact, in order to estimate a subset of the best $f = 10$ features², starting with $r = 4,520$ features would imply, if we want to test all the possible combinations, the following number of experiments:

$$n = \frac{r!}{f! * (r - f)!} = 9.7 \times 10^{29} \quad (1)$$

Assuming that a nonillion experiments are too many to be performed, a smarter approach had to be chosen. Therefore, we decided to apply a forward selection process (Mao 2004) as described in the following. The number of features used for the experiment was iteratively increased. In other words, to select the first best feature a kNN model for each of the $r = 4,520$ features was trained in a one dimensional feature space. Due to the memory limitations of the used hardware architecture, the feature selection was done by performing 100 kNN experiments, selecting for each of them a random subset of 20,000 data points, and using a 5-fold cross validation (see Sec. 2.3 for more details). The repeated experiments on different training samples were meant to generate statistics of the features in order to identify the most frequently selected ones. This was done to minimize the biases introduced by the random extraction of the training data. Since 100 runs were performed, sometimes more than one feature was selected. The basic idea behind the proposed strategy is to select a limited number of best performing features per step. The number of features which were actually selected were chosen by evaluating the occurrence of each of them as the best feature in all of the 100 runs. Therefore, for each iteration a minimum of one and a maximum of three features were selected. After choosing the best features, they have been fixed and the next run were performed in order to choose the subsequent features. This method has been iterated until the tenth feature was selected. A tree with a maximum branching number of three was derived, because in every step a maximum number of three features which

² The reason for selecting 10 features is discussed in Sec. 4.3 and Fig. 6

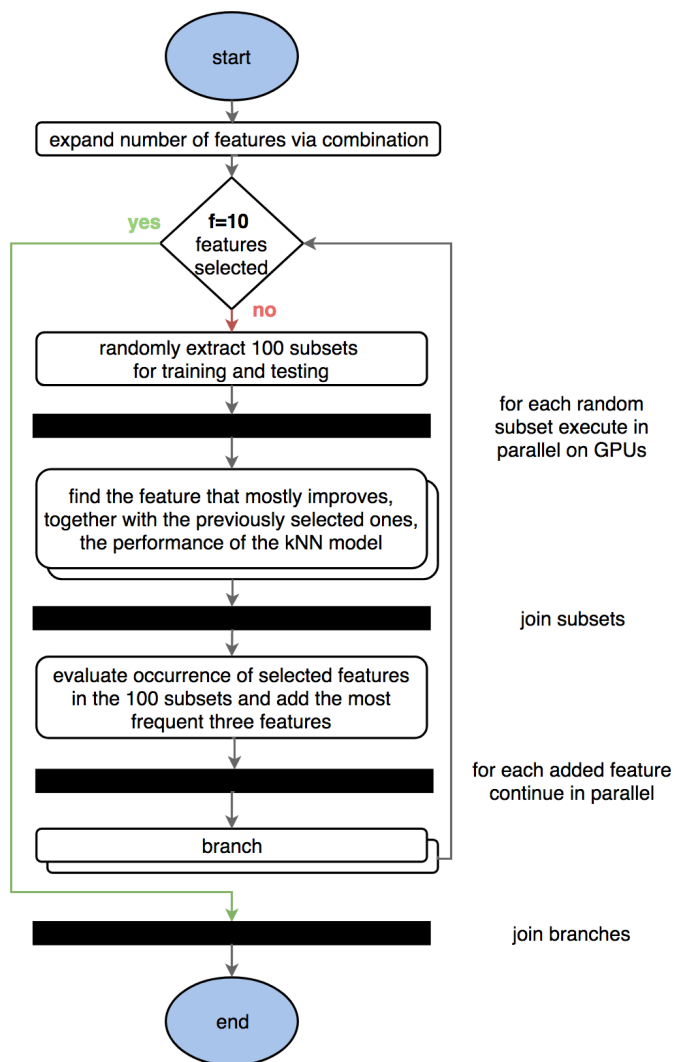


Fig. 1. The workflow used to generate the tree structure. The black boxes represent states where multiple operations are started in parallel or parallel operations are joined. The iteration is stopped when each branch of the tree has a depth of 10. A 5-fold cross validation is applied for every model evaluation step.

improve the model best were chosen. Each branch can be seen as a set of best performing feature combinations. The necessity of performing a high number of experiments on different data subsets is given by the slightly varying behavior of the kNN model with respect to different input patterns. The whole workflow is summarized in Fig. 1. The cross validation, moreover, was used in order to further reduce any risk of overfitting.

2.2.1. GPU parallelization for kNN

The feature selection is done by parallelizing the experiments on a GPU cluster. The massive use of GPUs proved to be mandatory in order to deal with such an amount of data, features, k values and runs on randomly sampled data-sets. Following Heineremann et al. (2013) and Gieseke et al. (2014), the kNN algorithm has been parallelized by using GPUs. Typically, GPU-based programs are composed by a host program running on CPU and a kernel program running on the GPU itself, which is parallelized on the GPU cores in several threads, or kernel instances. This scheme is particularly adapt for kNN models, due to the advantages obtained by parallelizing matrix multiplica-

tions. In the code used for this work (Gieseke et al. 2014) the calculation is performed by generating matrices containing the distances of the selected features from the query object. This calculation is entirely performed on the GPU, while the CPU is mainly used for synchronization and for updating a vector containing the selected features at every step. The approach based on this method proved to speed up the calculation of a factor of ~ 150 . We modified the given code to start the selection process with a given set of already selected features. This was done to enable the generation of the feature trees based on 100 random subsets.

2.3. Statistical estimators and Cross Validation

The results have been evaluated using the following set of statistical scores for the quantity $\Delta z = (z_{\text{spec}} - z_{\text{phot}})/(1 + z_{\text{spec}})$ expressing the estimation error³ on the objects in the blind validation set:

- bias: defined as the mean value of the normalized residuals Δz ;
- RMSE: root mean square error;
- NMAD: Normalized Median Absolute Deviation of the normalized residuals, defined as $NMAD(\Delta z) = 1.48 \times \text{median}(|\Delta z_i - \text{median}(\Delta z)|)$;
- CRPS: the continuous rank probability score (Hersbach 2000) is a proper score to estimate how well a single value is represented by a distribution. It is used following D’Isanto & Polsterer (2018).

The prediction of redshifts in a probabilistic framework has many advantages. The ability of reporting the uncertainty is the most important one to mention. In order to correctly evaluate the performance of the features in a probabilistic setting, the CRPS was added to the set of scores. By using the RF as a quantile regression forest and fitting a mixture of Gaussians to the predictions of the ensemble members, a probability distribution can be generated and the CRPS can be calculated. The DCMDN is by definition predicting density distribution that are represented by their mean when calculating the scores used for point estimates.

As stated before, all the indicators are then averaged on the k folds of the cross validation. Through this approach, also the standard deviation is obtained as a measure of the error on each statistical estimator. We do not report those values as the errors were small enough to be considered negligible. The cross validation (Kohavi 1995) is a statistical tool used to estimate the generalization error. The phenomenon of overfitting arises when the model is too well adapted to the training data. In this case, the performance on the test set will be poor as the model is not general enough. A validation set is defined, in order to test this generalization of the model, with respect to the training data, on an unseen and left out set of data. In particular, cross validation becomes necessary when dealing with small training sets or high dimensional feature spaces.

In this kind of approach, the data-set is divided in k subsets and each of them is used for the prediction phase, while all the $k - 1$ subsets constitute the training set. The training is then repeated k times, using all the subsets. The final performance is obtained by averaging the results of the single folds and the error on the performance is obtained by evaluating the standard deviation of the results coming from the different folds. In this work, we adopt a k -fold cross validation approach, with $k = 5$ for the kNN experiments and $k = 10$ for the RF experiments.

³ Note that Δz denotes the normalized error in redshift estimation and not the usually used plain error.

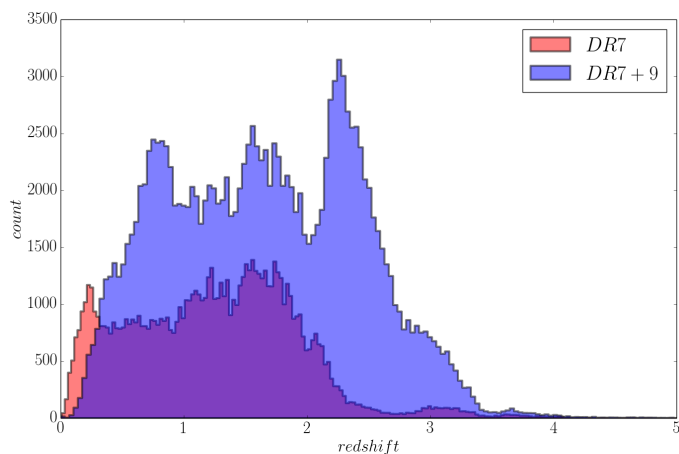


Fig. 2. Histogram showing the redshift distribution of the catalogs with objects from DR7 only and DR7 plus DR9. The distribution for the catalog DR7b is not reported here, because the difference with respect to catalog DR7a is practically negligible.

3. Data

In the following subsections the details about the data-set used and the feature combinations performed for the experiments are outlined.

3.1. Data-sets

The experiments are based on quasar data extracted from the SDSS DR7 (Abazajian et al. 2009) and SDSS DR9 (Ahn et al. 2012). Three catalogs have been retrieved for the experiments. Moreover, images for the DCMDN experiments have been downloaded making use of Hierarchical Progressive Survey (HiPS Fernique et al. 2015).

Catalog DR7a

Catalog DR7a is the most conservative with respect to the presence of bad data or problematic objects. It is based on DR7 only, with clean photometry and no missing data; the query used is reported in Appendix D. Furthermore, to be more conservative, we checked the spectroscopic redshifts in two different data releases (9 and 12) and we decided to cut all the objects with a discrepancy in z_{spec} not fulfilling the given criteria:

$$\begin{aligned} |z_{DR7} - z_{DR9}| &< 0.01, \text{ and} \\ |z_{DR7} - z_{DR12}| &< 0.01, \text{ and} \\ |z_{DR12} - z_{DR9}| &< 0.01 \end{aligned}$$

The final catalog contains 83,982 objects with a spectroscopically determined redshift.

Catalog DR7b

Catalog DR7b has been obtained using the same query used for Catalog DR7a, but removing the image processing flags. This has been done in order to verify if the presence of objects previously discarded by the use of these flags could affect the feature selection process. The catalog has been cleaned by removing all the objects with NaNs and errors bigger than a value of one, ending with a catalog containing 97,041 objects.

| | Magnitudes | σ | Radii | Ellipticities |
|----------|-----------------------|------------------|-----------------|----------------|
| | modelMag / Extinction | ✓ | devRad | devAB |
| | petroMag / Extinction | ✓ | expRad | expAB |
| | psfMag / Extinction | ✓ | petroRad | |
| | devMag / Extinction | ✓ | petroR50 | |
| | expMag / Extinction | ✓ | petroR90 | |
| Plain | 25 + 25 dereddened | 25 | 25 | 10 |
| Combined | 1,225 Differences | 300 Compositions | 300 Differences | 45 Differences |
| | 2,450 Ratios | | | 90 Ratios |
| Total | 4,520 | 3,725 | 325 | 145 |

Table 1. Types of features downloaded from SDSS and their combinations in order to obtain the final catalog used for the experiments. The number of each feature type is given alongside with the final number of synthetically derived features.

Catalog DR7+9

Catalog DR7+9 has been prepared mixing quasars from DR7 and DR9, in order to perform the feature selection with a different and more complete redshift distribution. The difference in the redshift distribution of the two catalogs can be seen from the histogram in Fig. 2. The catalog has been cleaned with the same procedure adopted for Catalog DR7b and the common objects between DR7 and DR9 have been used only once. This produced a catalog of 152,137 objects. In the following sections, the results obtained with this catalog are discussed in depth.

3.2. Classic features

In classic redshift estimation experiments for quasars and galaxies, as it can be found in the literature (e.g. D’Abrusco et al. 2007) for SDSS data, colors are mainly used as features. To be comparable, we decided to use a set of 10 features as our benchmark feature set. Colors of the adjacent filterbands for the point spread function (PSF) and model magnitudes are used together with the plain PSF- and model-magnitudes. In SDSS, the model magnitudes are the best fitting result of an exponential or de Vaucouleurs model. All Classic_{10} features can be found in the first column of Tab. 2.

3.3. Combined features

For each of the three catalogs, the features concerning magnitudes and their errors, radii, ellipticities and extinction are retrieved. An overview of the features is shown in Tab. 1. Magnitudes that have been corrected for extinction are denoted with an underline indicating that, e.g., $\underline{u}_{\text{model}}$ is equivalent to $u_{\text{model}} - u_{\text{extinction}}$. The parameter space has been enriched by performing several combinations of the original features (Gieseke et al. 2014). A similar feature generation approach was applied also in Polsterer et al. (2014) but with a limited set of plain features and combination rules. In other words, the magnitude features were combined obtaining all the pairwise differences and ratios, both in the normal and dereddened version. The errors on the magnitudes have been composed taking their quadratic sums. Finally, radii and ellipticities have been composed through pairwise differences with ratios only for the ellipticities. The final catalog consists of 4,520 features for each data item. It has to be noted, that the Classic_{10} features are of course included in this set of features. In Tab. 1, the types and amounts of the features obtained following this strategy are specified. As it appears from the table, the feature combinations can be divided in several groups:

- *simple features*: magnitudes, radii and ellipticities as downloaded from the SDSS database.

- *differences*: pairwise differences of the simple features; color indexes are a subset of this group utilizing only adjacent filters.
- *ratios*: ratios between the simple features; an important subset of this group is the one containing ratios between different magnitudes of the same filter; we will define this subset as *photometric ratios*.
- *errors*: errors on the simple features and their propagated compositions.

As we will see in the following, the *ratios* group, and its subgroup, the *photometric ratios*, are particularly important for the redshift estimation experiments.

4. Experiments and results

The feature selection has been performed applying the forward selection strategy, as described in Sec. 2.2, on the three catalogs. The verification of the resulting feature sets was performed using the RF. This algorithm is widely used in literature, and therefore the results obtained here can be easily compared to those with different feature selection strategies.

In addition, experiments using the classic features were performed, in order to compare their performances with the proposed selected features. Already in an early stage of the experiments, it turned out, that only four selected features are sufficient to achieve a performance comparable to classic features. Therefore the scores are always calculated separately for the full set of 10 selected features (*Best₁₀*) and the first four (*Best₄*) features only. To compare the results with a fully automated feature extraction and feature selection approach a DCMDN was used for the experiments, too.

It has to be noted that in some cases the same features sets have been found but exhibiting a different ordering. In these cases, all the subsets have been kept for the sake of correctness. In the next subsections the three experiments and the corresponding results are shown. The two experiments with Catalog DR7a and DR7b are designed to provide results that are comparable to the literature. For a scientifically more interesting interpretation, the less biased, not flagged and better representing Catalog DR7+9 was used for the main experiment. Therefore, only the results and performances of the first two experiments are given in a summarized representation, reserving more space for a detailed description of Experiment DR7+9. Further details concerning the results obtained with Catalog DR7a and DR7b are shown in Appendix A.

| Classic ₁₀ | DR7a Best ₁₀ | DR7b Best ₁₀ | DR7+9 Best ₁₀ |
|-------------------------|--|--|--|
| r_{psf} | i_{psf}/i_{model} | i_{psf}/i_{model} | i_{petro}/i_{psf} |
| r_{model} | g_{psf}/u_{model} | g_{psf}/u_{model} | $g_{psf} - u_{model}$ |
| $u_{psf} - g_{psf}$ | r_{psf}/i_{model} | r_{psf}/i_{model} | i_{exp}/r_{psf} |
| $g_{psf} - r_{psf}$ | i_{dev}/i_{psf} | i_{dev}/i_{psf} | $\sqrt{\sigma_{r_{model}}^2 + \sigma_{r_{dev}}^2}$ |
| $r_{psf} - i_{psf}$ | r_{psf}/g_{model} | z_{psf}/i_{model} | r_{psf}/g_{exp} |
| $i_{psf} - z_{psf}$ | i_{psf}/z_{model} | r_{psf}/g_{exp} | i_{psf}/z_{model} |
| $u_{model} - g_{model}$ | $r_{psf} - r_{petro}$ | $r_{psf} - r_{petro}$ | $i_{psf} - i_{dev}$ |
| $g_{model} - r_{model}$ | $\sqrt{\sigma_{r_{model}}^2 + \sigma_{g_{exp}}^2}$ | $i_{psf} - i_{petro}$ | r_{petro}/r_{psf} |
| $r_{model} - i_{model}$ | z_{model}/z_{psf} | z_{model}/z_{psf} | $i_{psf} - r_{model}$ |
| $i_{model} - z_{model}$ | $i_{psf} - i_{petro}$ | $\sqrt{\sigma_{g_{model}}^2 + \sigma_{g_{dev}}^2}$ | z_{exp}/z_{psf} |

Table 2. The classic and the best feature subsets obtained by the feature selection process of the experiments on the three catalogs. After the selection process, the RF was used to identify the feature branches of the corresponding trees that show the best performance.

| Exp | Set | # Features | mean | RMSE | NMAD |
|-------|-----------------------|------------|--------|-------|-------|
| DR7a | Classic ₁₀ | 10 | -0.024 | 0.163 | 0.051 |
| | Best ₄ | 4 | -0.023 | 0.163 | 0.080 |
| | Best ₁₀ | 10 | -0.014 | 0.124 | 0.044 |
| | DCMDN | 65,536 | -0.020 | 0.145 | 0.043 |
| DR7b | Classic ₁₀ | 10 | -0.030 | 0.180 | 0.059 |
| | Best ₄ | 4 | -0.027 | 0.183 | 0.087 |
| | Best ₁₀ | 10 | -0.019 | 0.145 | 0.050 |
| | DCMDN | 65,536 | -0.024 | 0.171 | 0.032 |
| DR7+9 | Classic ₁₀ | 10 | -0.033 | 0.207 | 0.073 |
| | Best ₄ | 4 | -0.032 | 0.206 | 0.100 |
| | Best ₁₀ | 10 | -0.023 | 0.174 | 0.060 |
| | DCMDN | 65,536 | -0.027 | 0.184 | 0.037 |

Table 3. Summary of the scores obtained with the RF and DCMDN models in the three experiments. The DCMDN automatically extracted 65,536 features for each experiment. The resulting scores are given, too.

| DR7a | CRPS | DR7b | CRPS | DR7+9 | CRPS |
|-----------------------|-------|-----------------------|-------|-----------------------|-------|
| Classic ₁₀ | 0.110 | Classic ₁₀ | 0.131 | Classic ₁₀ | 0.167 |
| Best ₄ | 0.154 | Best ₄ | 0.172 | Best ₄ | 0.203 |
| Best ₁₀ | 0.089 | Best ₁₀ | 0.106 | Best ₁₀ | 0.140 |
| DCMDN | 0.099 | DCMDN | 0.124 | DCMDN | 0.146 |

Table 4. Table showing the performance of the different feature subsets respect to the CRPS score for the three catalogs.

4.1. Experiment DR7a

The feature selection on the Catalog DR7a produced 22 subsets of 10 features each. Only 20 features, of the initial 4,520, compose the tree. The three features:

- g_{psf}/u_{model}
- i_{psf}/z_{model}
- z_{model}/z_{psf}

appear in all the possible branches. For all presented feature sets, the RF experiments have been performed. The best performing 10 features are indicated in the second column of Tab. 2 (DR7a subset) in the order of their occurrence. The performances are compared with the results of the Classic₁₀ features presented in the first column of the same table. A summary of the most important results is shown in the first section of Tab. 3. As it is shown in Tab. 3, the experiment with the Best₁₀ subset outperforms the experiment with the Classic₁₀ features with respect to all the statistical scores.

Moreover, in Tab. 3 the results obtained using the DCMDN are shown, in order to compare the predictions with a model based on automatic features selection. The DCMDN model automatically extracts 65,536 features from images in the five filters *ugriz* of size $16 \times 16 \text{ pixel}^2$. This model is meant to generate probability density functions (PDFs) in the form of Gaussian Mixtures instead of point estimates. Therefore, in order to calculate the scores, the weighted mean of every PDF with respect to the mixture components has been estimated. As shown in the table, the performance is superior with respect to the Classic₁₀ features and the Best₄ subset, but it is outperformed by the Best₁₀ subset of features. The performance of these four sets have been compared using the CRPS score, as it is reported in the left section of Tab. 4. Those results are consistent with the previously found results. A detailed listing of the results is given in Appendix A with the individual feature tree being visualized as a chord diagram (Krzywinski et al. 2009).

4.2. Experiment DR7b

In the experiment performed with Catalog DR7b, the proposed model selected 26 features generating 41 subset combinations. Only the following two features appear in all the subsets:

- i_{psf}/i_{petro}
- g_{psf}/u_{model}

From the RF validation runs, the subset reported in the third column of Tab. 2 (DR7b) produces the best performance. The most important results are shown in the second section of Tab. 3, in which the results obtained with the previous experiment (DR7a) are confirmed. This is valid considering both the RMSE and the CRPS indicators. The CRPS is shown in the middle section of Tab. 4. Therefore, the performance given using the $Best_{10}$ subset is superior with respect than adopting the $Classic_{10}$ features. The DCMDN model is outperformed too. Several features can be found in both experiments with the catalogs DR7a and DR7b and the general structure of the tree between the two experiments is comparable. Therefore, the exclusion of photometric flags seems not to affect substantially the global process of feature selection. It can be noticed, however, that the general performance degrades. This is due to the increased presence of object characterized by a less clean photometry. The detailed feature selection results for this experiment and the chord diagram are also shown in Appendix A.

4.3. Experiment DR7+9

The feature selected from the Catalog DR7+9 are shown in Tab. 5. In Fig. 3 a chord diagram is given to visualize the structure of the individual subsets. In this experiment the model selected 14 individual features grouped in 9 subsets. Due to the different redshift distribution, different features are selected with respect to the previous experiments. The following six features are in common between all the subsets:

- $i_{psf} - i_{dev}$
- i_{psf}/z_{model}
- $g_{psf} - u_{model}$
- i_{petro}/i_{psf}
- r_{psf}/g_{exp}
- i_{exp}/r_{psf}

The best performing subset is shown in the fourth column of Tab. 2 (DR7+9 subset), while in the third section of Tab. 3 results obtained with the RF experiments are given. Moreover, in the right section of Tab. 4 the results with the CRPS as indicator are provided. For this experiment we also report the z_{spec} vs z_{phot} plots in Fig 4. This classical representation visualizes the better concentration along the ideal diagonal for both, the $Best_{10}$ features as well as the features derived through the DCMDN. When using the features in a probabilistic context, the better performance with respect to outliers of the DCMDN can be observed (Fig 5). The probability integral transform (PIT Gneiting et al. 2005) histograms show very similar performances for all the feature sets that had been selected. Besides the outliers, the estimates are sharp and well calibrated, exhibiting no difference in comparison to the results generated with the $Classic_{10}$ features. This is good indication, that no systematic biases were added through the selection process.

Finally, the performance obtained with the $Classic_{10}$ features is compared to the ones achieved with the $Best_{10}$ features in a

cumulative way. In Fig. 6, the RMSE and the NMAD are plotted with respect to the used number of features of the $Best_{10}$ set. This is important in order to show that starting with the 4th feature, the model reaches already a performance comparable with the $Classic_{10}$ features. Originating in the random data sampling during the selection process, the resulting different feature subsets do not show obvious differences in the quality of the final performance. In fact, the results obtained with the $Best_{10}$ subset are far better with respect to the performance obtained using the $Classic_{10}$ features and the DCMDN. This is a confirmation of the quality and strength of the proposed method.

5. Discussion

In the following subsections we discuss in detail the features found with the proposed method, the improvement in performance of the photometric redshift estimation models in comparison to the classic features and the physical interpretation of the selected features.

5.1. Features

The results obtained from the feature selection process for the three experiments demonstrate that most of the information can be embedded in a limited number of features, with respect to the initially generated amount of pairwise combinations. The following four features have been selected and are in common between all the three experiments:

- $r_{psf} - r_{petro}$
- $i_{psf} - i_{dev}$
- i_{psf}/z_{model}
- r_{psf}/i_{exp}

This is a clear indicator that those features contain some essential information. Besides noting that they encode a spatial/morphological characteristic, we have no clear explanation. Some features, as it will be analyzed in the next sections, can be clearly connected to physical processes occurring in the considered sources. Other features are instead much harder to be interpreted, which demands a deeper analysis in the future. Given that photometric redshifts are just used as testbed for the proposed methodology, such an analysis is beyond the scope of this work. A quick and shallow inspection of the features exhibits that the *ratios* and *differences* play a major role. In Tab. 5 for the experiment DR7+9 the different groups of features are highlighted using different background patterns. This visually summarizes the dominant occurrence of those groups. In fact, all the features except the 4th (*errors*) belong to one of these two groups. Moreover, the individual branches of feature sets employ a feature of the same group for the first seven positions, showing a great stability in the composition of the branches. The experiment based on the DR7+9 catalog generates a much less complex structure of the tree of feature sets, with respect to the experiments DR7a and DR7b. Less branches and a reduced number of features are selected. Reasons for this behavior are the more complete redshift distribution of the catalog DR7+9 with respect to the other two and the improvement in the SDSS photometry from DR7 to DR9. This drives the model to find the required information in a reduced number of efficient features. The analysis of the tree composition and features distribution can be done following the chord diagram shown in Fig. 3. The chord diagram is an optimal visualization tool for the description of a complex data structure. In this diagram, every feature is associated to a specific color,

| id | Feature 1 | Feature 2 | Feature 3 | Feature 4 | Feature 5 | Feature 6 | Feature 7 | Feature 8 | Feature 9 | Feature 10 | |
|----|-----------------------------------|-------------------------------------|---------------------------------|--|---------------------------------|-----------------------------------|-----------------------------------|-----------------------------------|-------------------------------------|-------------------------------------|-------------------------------------|
| 1 | $i_{\text{petro}}/i_{\text{psf}}$ | $g_{\text{psf}} - u_{\text{model}}$ | $i_{\text{exp}}/r_{\text{psf}}$ | $\sqrt{\sigma_{r_{\text{model}}}^2 + \sigma_{r_{\text{dev}}}^2}$ | $r_{\text{psf}}/g_{\text{exp}}$ | $i_{\text{psf}}/z_{\text{model}}$ | $i_{\text{psf}} - i_{\text{dev}}$ | $r_{\text{petro}}/r_{\text{psf}}$ | $i_{\text{psf}} - i_{\text{dev}}$ | $z_{\text{psf}} - z_{\text{model}}$ | |
| 2* | | | | | | | | | $z_{\text{exp}}/z_{\text{psf}}$ | | |
| 3 | | | | | | | | | $i_{\text{psf}} - r_{\text{model}}$ | | |
| 4 | | | | | | | | | $i_{\text{psf}} - i_{\text{dev}}$ | | |
| 5 | | | | | | | | | $r_{\text{psf}}/g_{\text{exp}}$ | $r_{\text{petro}}/r_{\text{psf}}$ | $i_{\text{psf}} - i_{\text{dev}}$ |
| 6 | | | | | | | | | $r_{\text{psf}}/g_{\text{exp}}$ | $i_{\text{psf}} - i_{\text{dev}}$ | $z_{\text{psf}} - z_{\text{model}}$ |
| 7 | | | | | | | | | $z_{\text{psf}} - z_{\text{model}}$ | | |
| 8 | | | | | | | | | $r_{\text{petro}}/r_{\text{psf}}$ | $i_{\text{psf}} - i_{\text{dev}}$ | |
| 9 | | | | | | | | | $r_{\text{psf}} - r_{\text{petro}}$ | | |

Table 5. Detailed feature branches obtained from the feature selection for the DR7+9 experiment. The 2nd branch, indicated with the * symbol, is the best performing subset with respect to the experiments using the RF. The ratios and photometric ratios are indicated, respectively, with vertical lines and dots. The differences are with horizontal lines and the errors are with north west lines. The color code for the features is the same as shown in the chord diagram in Fig. 3.

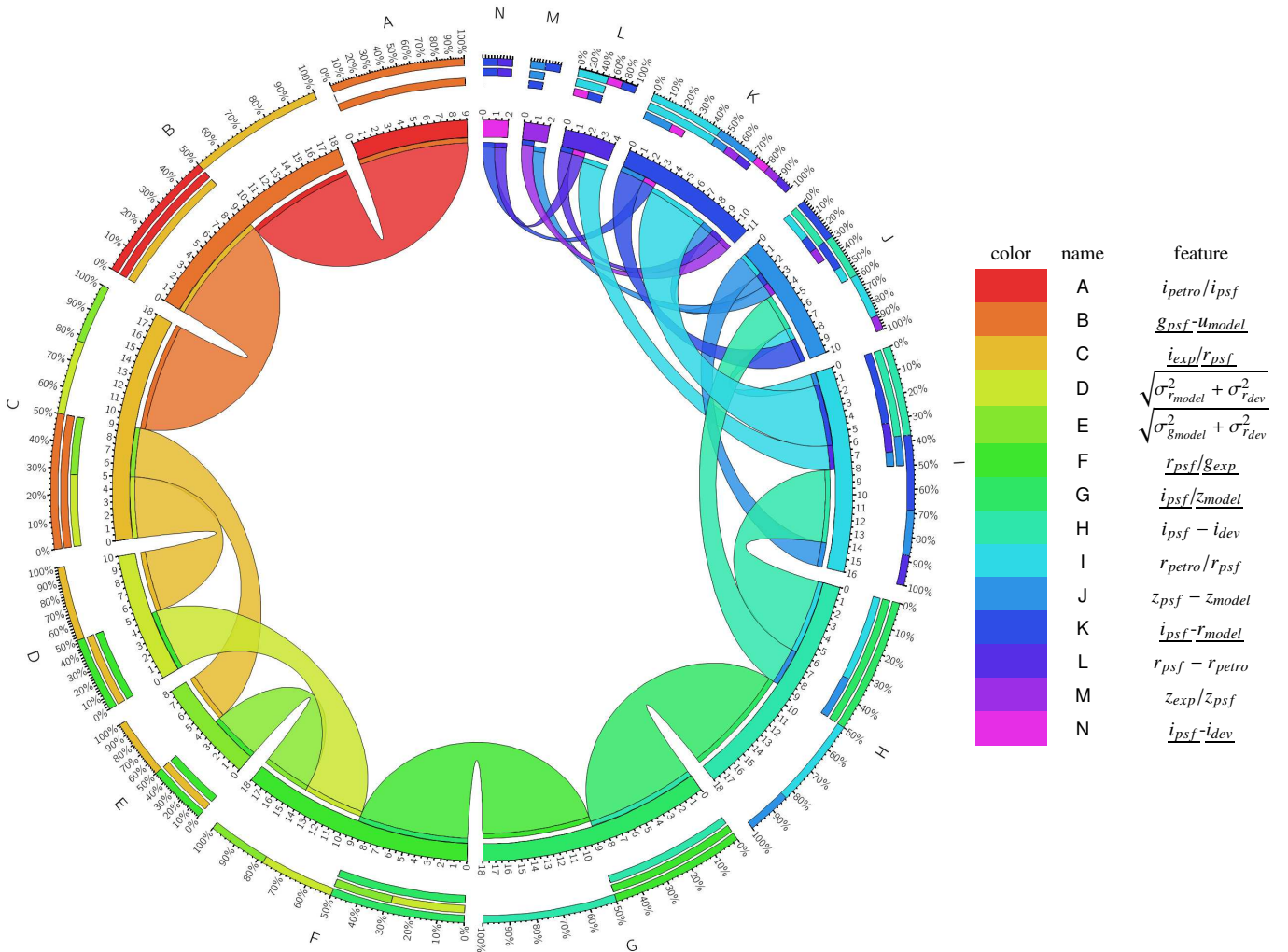


Fig. 3. Chord diagram of the features derived in Experiment DR7+9. Every feature is associated to a specific color, and starting from the first feature A it is possible to follow all the possible paths of the tree, depicting the different feature subsets. Ordered from outside to inside, the external arcs represent the occurrences of a particular feature: the total percentage of the individual connections, the numbers and sources of connections entering, and the numbers and targets of connections exiting. (Note the branches splitting in feature C and re-joining in feature F)

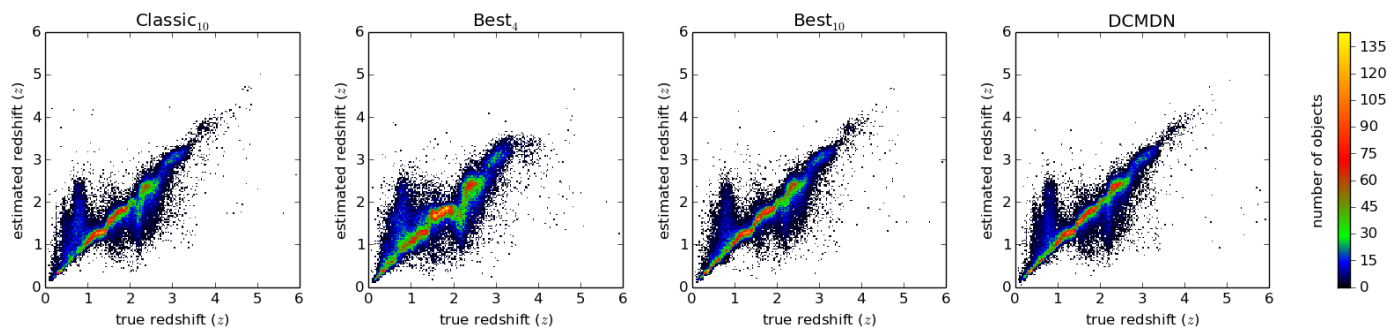


Fig. 4. Comparison of the spectroscopic (true) redshifts (z_{spec}) against the photometrically estimated redshifts (z_{phot}) of the different feature sets in experiment DR7+9.

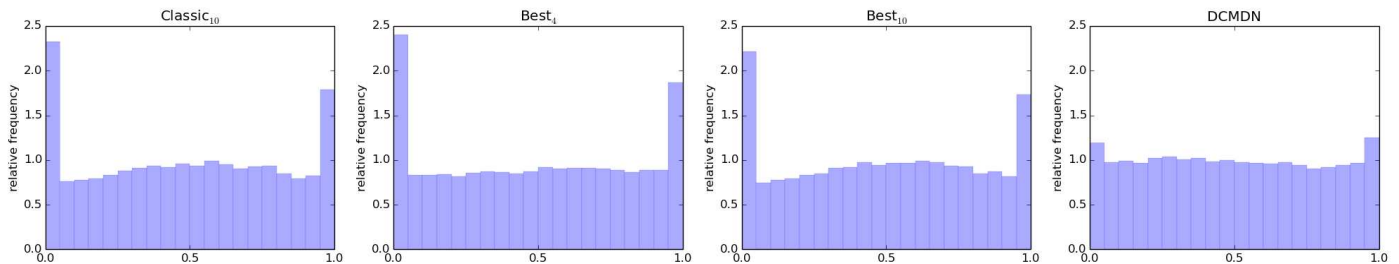


Fig. 5. PIT histograms for experiment DR7+9 for the different features sets, as shown in Tab. 4. Except the PIT of the DCMDN, all other feature sets generate results with significant outliers at the extrema.

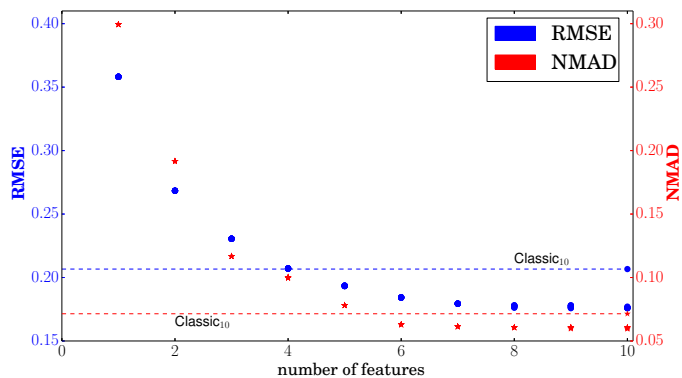


Fig. 6. Comparison of model performance with regard to the number of used features. The root mean square error and normalized median absolute deviation of the results from the DR7+9 RF experiments are presented. As reference line the performance achieved with the $Classic_{10}$ features is shown. As it can be seen, from the fourth feature on, the performance of the subsets, outperforms the $Classic_{10}$ features. After the ninth feature, the improvement settles. When adding many more features, the performance will start to degrade.

and starting from the first feature (A) it is possible to follow all the possible paths of the tree, depicting the different feature subsets. Ordered from outside to inside, the external arcs represent the occurrences of a particular feature: the total percentage of the individual connections, the numbers and sources of connections entering, and the numbers and targets of connections exiting. Therefore, the chord diagram, coupled with Tab. 5, gives a clear description of the structure and composition of the tree of features. In addition, in Tab. 5 the same color code as in the chord diagram is adopted, to identify the features and their distribution. The chord diagram nicely visualizes that the feature trees are splitting at feature C and later rejoin at feature F. In comparison to the chord diagram obtained for Experiment DR7+9, the

two chord diagrams for the experiments DR7a and DR7b (see Appendix A), immediately visualizes the higher complexity of those trees. From Fig. 3 and Tab. 5 it appears that, apart some few exceptions, the selected features follow a precise scheme. No classic color indexes or any of the $Classic_{10}$ features have been chosen, while only differences between different magnitudes of the same band or differences between different type of magnitudes play a certain role. The *ratios* have been all selected in the extinction corrected version, except for the subcategory of the *photometric ratios*. This can be understood considering that the latter are ratios between magnitudes of the same filter where the contribution of the extinction correction tends to cancel out.

Another relevant aspect in experiment DR7+9 is that all the 15 features in the tree are exclusively a composition of magnitudes and their errors. Neither radii nor ellipticities have been chosen during the selection process. As just quasars have been used in the experiments, this introduces a bias to the selection process in favor of magnitudes and against shape based features. This is a clear indication that just the magnitudes are required to describe the objects and explore the parameter space in the setting of photometric redshift estimation. Although *photometric ratios* are shape-related parameters, they express the ratio between the centered and the extended part of a component that can be interpreted as flux of the hosting galaxy. Therefore, here a bias introduced by using quasars for the experiments can not be observed.

It is remarkable that photometric errors are selected as features, given that there is no obvious physical relation between the redshift of the considered objects and the measurement errors reported by the photometric pipeline of SDSS. Hereby it is important to consider how errors are derived in the SDSS, based on flux measurements (?). Magnitude errors quantify the discrepancy between the fitted photometric model (psf, model, petrosian, etc.) and the observed pixel-wise distribution of spatially correlated fluxes, with respect to the applied noise model. Therefore, it is evident that the errors on the single magnitudes

appear to be larger for fainter objects, a physical property that is directly correlated to distance. In addition, the deviation of spatial flux distributions from the applied spatial photometric models are good morphological indicators, e.g. shape and size of the hosting galaxy are correlated with redshift. The workflow adopted is able to capture these dependencies, selecting a composition of errors as an important feature of the best set.

Even though 4,520 features have been synthetically created by combining base features, only 15 were selected in experiment DR7+9 (19 and 26 for experiments DR7a and DR7b, respectively). Furthermore, some features encode the same type of information with just subtle differences in composition. It is remarkable that every features that is build on magnitudes incorporates a PSF magnitude. Moreover, the model and exp magnitude in the SDSS are related⁴, with the model magnitude being just the better fitting model comparing an exponential and a de Vaucouleurs profile. In the first stages of the selection process, the proposed algorithm does not select differing branches but identifies essential features to produce good results when photometrically estimating redshifts. These observations are also valid for the results found in experiments DR7a and DR7b.

5.2. Comparison of performance

Using the RF, the validation experiments were carried out on every feature set. The second subset, indicated as Best_{10} , gave a slightly better performance than the others. Even though we would not consider this as a substantial effect, we decided to choose this as our reference set. It can be noticed from Fig. 6 that from the 4th feature on, every subset delivers a performance comparable to the performance of all ten features in the Classic_{10} set, with respect to the RMSE. Consistently, the usage of more than four feature outperforms the Classic_{10} , independently of the subset used. Adding more features improves further the performance and the trend becomes asymptotic around the 9th feature. At a certain point, adding many more features results in a degradation of the redshift estimation performance. After the 8th feature, the contribution is of minor nature. Just to have a fair comparison to the Classic_{10} features we decided to pick the same number of ten features, even though already a smaller number is sufficient to outperform the Classic_{10} features. The performance improvement is evident seeing the results reported in Tab. 3 and Fig. 4. It is important to note that the CRPS results (Tab. 4) confirm the performance shown with respect to the other scores. When predicting PDFs instead of point estimates, the PIT histograms (Fig. 5) indicate the DCMDN as the best calibrated model. This result is reasonable, because the DCMDN is the only model trained using the CRPS as loss function, which is focused on the PDFs calibration. The kNN and the RF are instead based on optimization of point estimates using the RMSE. Therefore, the calibration of the PDFs estimated using the DCMDN is superior. The use of such a probabilistic model is helpful to handle the presence of extreme outliers, since it is not based on the minimization of the RMSE, as discussed in D’Isanto & Polsterer (2018). The usage of PDFs allows to identify objects with an ambiguous redshift distribution, while in a point estimation scenario, where just the mean of such a distribution would be considered, the estimates of those objects would result in extreme outliers.

Six features of the best subset are ratios of different magnitudes. Three of them are plain *ratios*, while three are *photometric ratios*. Analyzing the fourth column of Tab. 2, it appears that one

| Exp. | catalog DR7a | catalog DR7b | catalog DR7+9 |
|-------|--------------|--------------|---------------|
| DR7a | 0.124 | 0.146 | 0.176 |
| DR7b | 0.125 | 0.145 | 0.176 |
| DR7+9 | 0.124 | 0.147 | 0.174 |

Table 6. Cross experiments performed with the RF, using the Best_{10} sets obtained from every experiment with all the three catalogs. The results are expressed using the RMSE. It can be noticed the negligible difference of performance, for every catalog, independently from the feature set used.

of the components of these features is always a PSF magnitude, coupled with a model, petro or exp magnitude. Therefore, from the analysis of the results obtained, we can state that the reason for the performance improvement is not in the choice of some specific features, or in a particular subset of features, but in their type and in the combination of certain groups.

All these aspects are clear indicators to state the following two conclusions. The proposed method is highly stable, permitting to derive subsets of features which are equivalently good performing and similar, based on a common structure. In this sense, the improvement with respect to the use of Classic_{10} features is clear. In order to prove the robustness of the proposed method we performed some experiments using for each dataset the Best_{10} features obtained with the other two catalogs, as shown in Tab. 6, and the results were almost as good as in the other cases. The method captures the inherent structure of the physical properties of the sources which is essential to provide good photometrically estimated redshifts for quasars.

5.3. Physical interpretation

In contrast to deep learning models, feature based approaches have the advantage of allowing an interpretation in a physical context. Therefore the features selected by our approach are discussed in the following. By analyzing the importance of each feature of the Best_{10} set in smaller redshift bins, the contribution of certain spectral features can be understood. In Fig. 7 the importance is presented for sliding bins of $\Delta z = 0.2$ based on the Gini index (Breiman et al. 1984). The Gini index is used in the RF to perform the segmentation of the parameter space orthogonally to its dimensions at every node. As all ten features contribute individually, the total contribution is normalized to one and the individual lines are presented in a cumulative way. The relative importance of each feature is clearly not reflecting their ordering, as they have been assembled by a forward feature selection algorithm. In particular, the first feature of the best set does not show a dominant role when using multiple features. When building a photometric regression model based on just a single feature, the concentration index in the i band provides the best tracer for distance. Therefore a concentration index in the i band is consequently chosen in all the three experiments. This selection is of course heavily biased by the distribution of our training objects with respect to redshift and the fact that objects for training are selected based on the classification of the spectral template fitting of SDSS. As soon as more photometric features are used, the spectral energy distribution and distinct spectral features are the dominant source of information for estimating the redshifts. Those features are mainly *ratios*. To use ratios instead of colors is a surprising fact, as in literature, colors are the usual choice for photometric redshift estimation models. In Fig. 7 one can inspect how the different features contribute at different redshift bins, building a well performing model that covers the full redshift range. Besides some very narrow redshift

⁴ <http://classic.sdss.org/dr7/algorithms/photometry.html#magmodel>

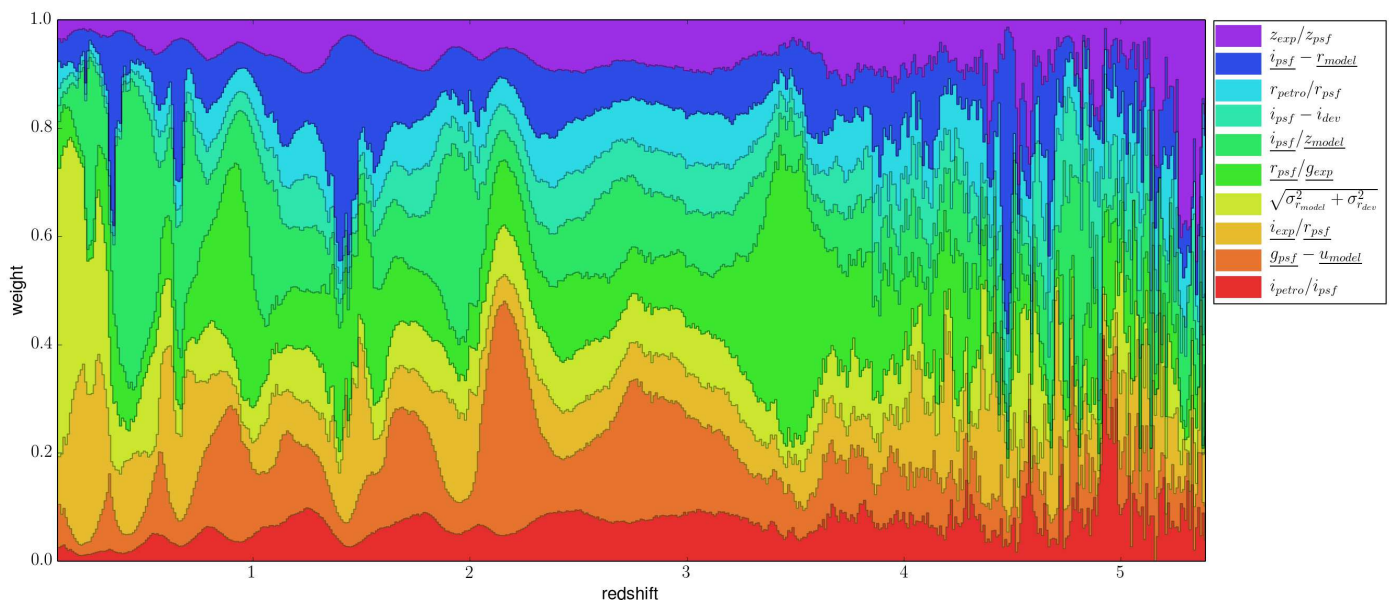


Fig. 7. Importance of every feature of the Best_{10} subset from experiment DR7+9. For a sliding redshift bin of $\Delta z = 0.2$, the importance of every feature was calculated in a localized regression model based on the Gini index as utilized by the RF. The color code used is the same adopted for the chord diagram in Fig. 3.

regions, no clear structure with preference of some photometric features can be observed at higher redshifts ($z > 4$). This is due to the poor coverage of the training and validation data in that range. The ordering of the features in the Best_{10} set and their importance as shown in Fig. 7 can be compared with the global feature importance as obtained from the RF experiment (Tab. 7). The feature importance calculated on the overall redshift distribution gives different indications with respect to the bin-wise analysis, but it is quite consistent with the original order obtained from the feature selection. This is a further demonstration of the stability and robustness of the proposed method.

The different behaviors and importance found for the features in the individual redshift bins can be partially explained by analyzing distinct features in the spectral energy distribution. By carefully inspecting the emission lines of quasars as reported by the SDSS spectral pipeline, a connection between some photometric features and emission lines could be found. Those features that are composed of adjacent filter bands are very sensitive for spectral lines that are in the vicinity of the overlapping area

of filter transmission curves. This can be explained by a flipping of the feature, e.g. positive/negative for colors or above/below one for ratios. Already a little shift of an emission line with respect to the redshift is enough to create a significant change in the feature space, that is detected and utilized by the machine learning model. Five features of the Best_{10} share this characteristic. Therefore the discussion with respect to emission lines is focused on selected features that are composed of magnitudes from neighbouring filter bands. Using the well known relation:

$$z = \frac{\lambda_{\text{observed}}}{\lambda_{\text{emitted}}} - 1 = \frac{\lambda_{\text{filter intersection}}}{\lambda_{\text{qso emission line}}} - 1 \quad (2)$$

it is possible to calculate the redshift at which a specific emission line becomes traceable when using a certain filter combination. The proposed features capture many distinct emission lines, showing peaks in the redshift bins where the lines appear. This is shown in Fig. 8-9, where the feature importance has been compared with the classic features of the corresponding bands. To understand better the influence of the usage of magnitudes describing extended objects, both, the PSF and the model magnitudes of the classic features where used for comparison. In Fig. 8 the comparison is performed with respect to PSF colors, while in Fig. 9 the same comparison is done with respect to model colors. By using Eq. 2, a selected set of spectral emission lines of quasars has been convolved with the corresponding filter characteristics to annotate the plots. Besides the maximum of the overlapping region, the start and the end of the intersection are depicted. We defined the upper and lower limits as the points in which the sensitivity of the filter curve is equal to 0.001 in quantum efficiency. It can be noticed that many emission lines are perfectly corresponding to peaks in importance exhibited by the features of the Best_{10} set. This can be observed only partially for the classic features.

In particular, purely PSF or model magnitude based colors have a different and often complementary contribution for several spectral lines. This is due to the fact that either concentrated or extended characteristics of the analyzed objects are considered. The proposed features are more suitable than classic fea-

| Position | Feature | Score |
|----------|---|-------|
| 1 | ▲1 $\frac{g_{psf} - u_{model}}{i_{petro}/i_{psf}}$ | 0.424 |
| 2 | ▼1 $\frac{i_{petro}/i_{psf}}{\sqrt{\sigma_{r_{model}}^2 + \sigma_{r_{dev}}^2}}$ | 0.121 |
| 3 | ▲1 $\frac{i_{exp}/r_{psf}}{r_{psf}/g_{exp}}$ | 0.092 |
| 4 | ▼1 $\frac{r_{psf}/g_{exp}}{i_{psf}/z_{model}}$ | 0.072 |
| 5 | ≡ $\frac{i_{psf}/z_{model}}{i_{psf} - r_{model}}$ | 0.071 |
| 6 | ≡ $\frac{i_{psf} - r_{model}}{i_{psf} - i_{dev}}$ | 0.064 |
| 7 | ▲2 $\frac{i_{psf} - i_{dev}}{z_{exp}/z_{psf}}$ | 0.062 |
| 8 | ▼1 $\frac{z_{exp}/z_{psf}}{r_{petro}/r_{psf}}$ | 0.042 |
| 9 | ▲1 r_{petro}/r_{psf} | 0.026 |
| 10 | ▼2 r_{petro}/r_{psf} | 0.025 |

Table 7. The features of the Best_{10} set from experiment DR7+9, ordered by decreasing importance as expressed by the score of the RF based on the Gini criterion. The change with respect to the initially found ordering of the presented approach, and the RF score are reported, too.

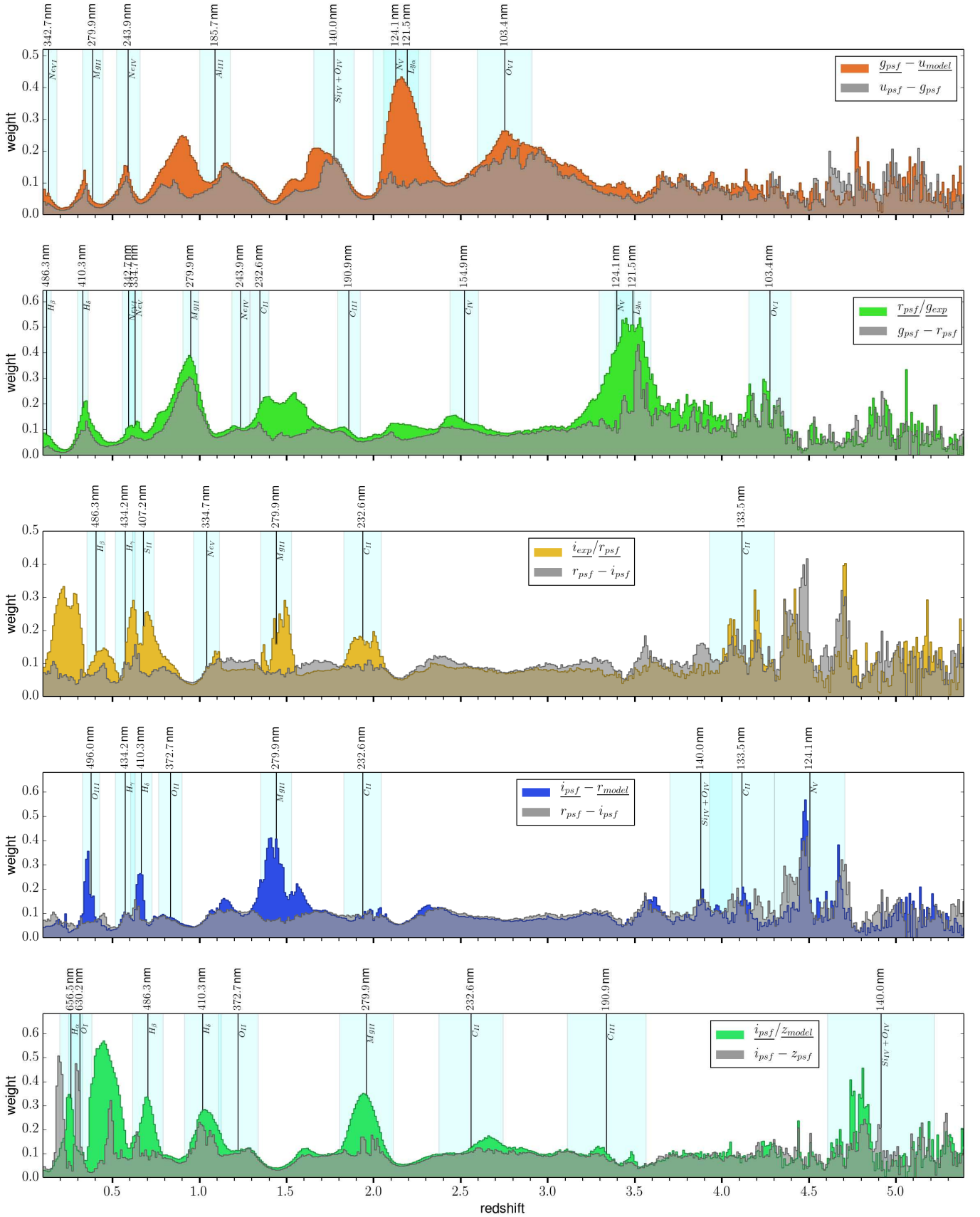


Fig. 8. Feature importance of the five features from the *Best*₁₀ set composed by magnitudes from neighbouring bands. As in Fig. 7, for a sliding redshift bin of $\Delta z = 0.2$, the importance of every feature was calculated. The results are compared to the classic features using PSF magnitudes of the same bands. Based on the characteristics of the *ugriz* filters, the wavelengths indicating the start, center and end of the overlapping regions are used to overplot the positions of particular quasar emission lines using Eq. 2. The used color code is the same as in Fig. 3, while corresponding features of the *Classic*₁₀ set are always shown in grey.

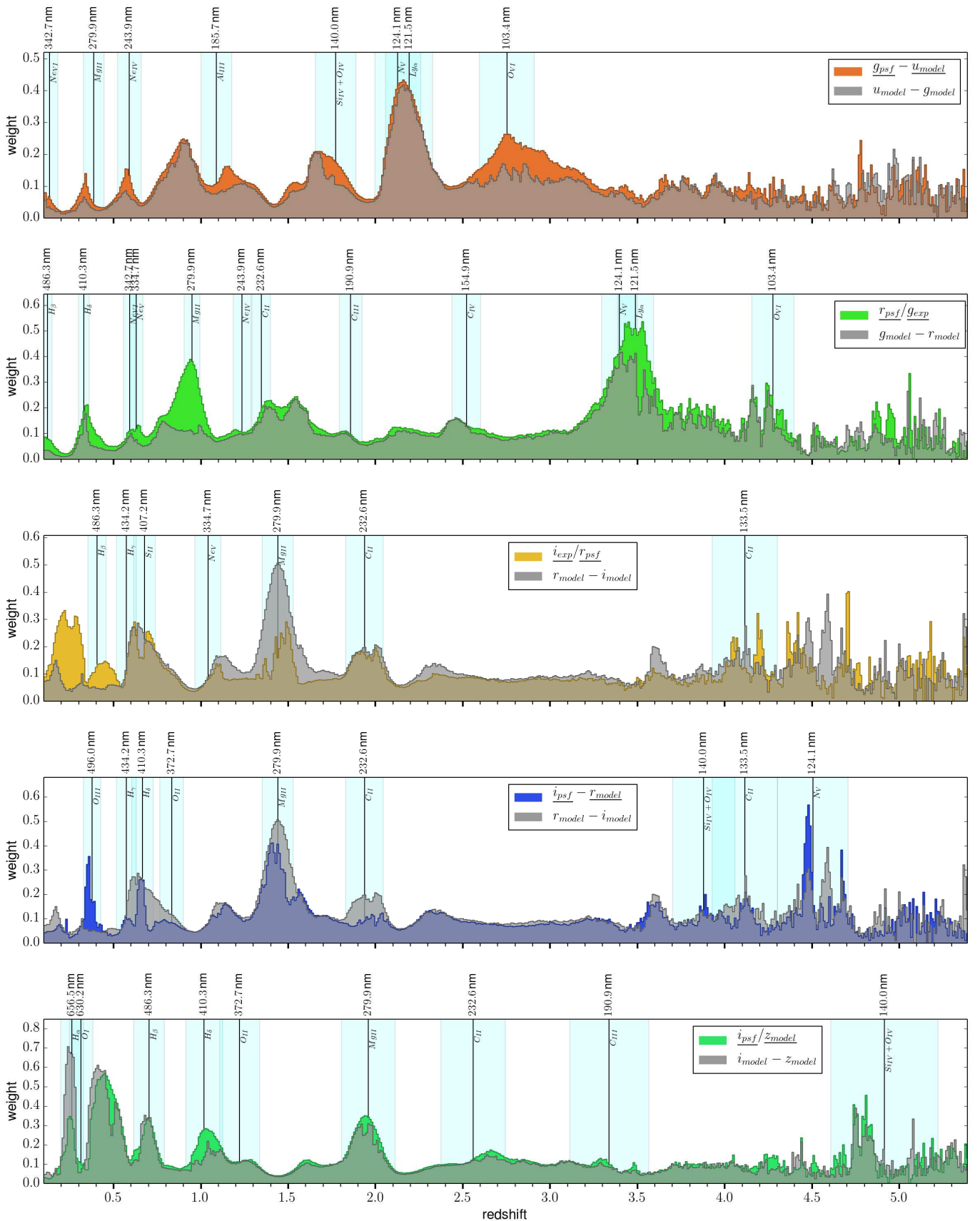


Fig. 9. Feature importance of the five features from the $Best_{10}$ set composed by magnitudes from neighbouring bands. As in Fig. 7, for a sliding redshift bin of $\Delta z = 0.2$, the importance of every feature was calculated. The results are compared to the classic features using model magnitudes of the same bands. Based on the characteristics of the $ugriz$ filters, the wavelengths indicating the start, center and end of the overlapping regions are used to overplot the positions of particular quasar emission lines using Eq. 2. The used color code is the same as in Fig. 3, while corresponding features of the $Classic_{10}$ set are always shown in grey.

tures to describe the peaks at distinct emission lines. Considering the $N_V - Ly_\alpha$ lines for the $g_{psf} - u_{model}$ feature, the comparison between the extended and concentrated classic features clearly indicates that an extended component of the source is captured via this feature. Keeping in mind that a pixel size of $0.4''$ of the SDSS camera corresponds⁵ at a redshift of $z \approx 2.2$ to ≈ 3.4 kpc, this is a clear indicator that the hosting galaxy is significantly contributing to the solution of the photometric redshift estimation model. A similar behaviour can be observed for the $N_V - Ly_\alpha$ lines in the r_{psf}/g_{exp} feature, while the Mg_{II} emission line is mainly appearing in the PSF color. Therefore the Mg_{II} emission line can be considered to be more prominent in the central region of the objects. Between the most notable lines, the Lyman- α and the Balmer series can be identified. Other important lines found are the C_{II} , C_{III} , C_{IV} , O_I , O_{II} , O_{III} , O_{VI} and the Mg_{II} lines. Besides the identified peaks caused by specific emission lines, some peaks in weight stay unexplained. Even though it is possible to distinguish between mostly spatially extended or concentrated characteristics of the objects, an association of a single emission line fails. In those cases not the transition of a line between two filters, but an overall shape relation is captured by the selected parameters. As the selected features combine the strength of identifying line transitions as well as morphological characteristics, the resulting boost in performance of the photometric redshift estimation model can be well explained. To explain the meaning of the selected feature that use a combination of features extracted from the same photometric band and thereby describe a morphological structure of the source, further image based investigations are necessary. This proves that a model using the proposed feature selection approach is better able to exploit the information which is representing the underlying physical/morphological structure as well as the processes going on in the sources.

6. Conclusions

In this work a method to select the best features for photometric redshift estimation is proposed. The features are calculated via a greedy forward selection approach, in which the features are selected from a set of 4,520 combinations based on the photometric and shape information stored in the SDSS DR7 and DR9 catalogs. By randomly sampling the training data and running multiple kNN experiments, trees in which every branch constitutes a subset of features were generated for all the experiments. The obtained branches have then been validated using a RF model and compared to the results obtained using classic sets of features. Moreover, the results have been compared with a convolutional neural network based model, meant to automatically perform the feature extraction and selection. Three experiments, based on different catalogs, have been done. The first catalog is obtained selecting quasars from SDSS DR7 and applying photometric flags. The second catalog is composed by quasars from SDSS DR7 too, but without using photometric flags. Finally, the third catalog is made by mixing SDSS DR7 and DR9 quasars, in order to extend the redshift distribution. We have shown that all the sets obtained in all the experiments outperform the Classic₁₀, and in particular a best performing branch has been identified for each catalog. The best sets are also giving better performance with respect to the automatic model, even though the latter typically shows a better calibration and is less affected by outliers, when predicting PDFs instead of point estimates. The new best features obtained in the present work are

not immediately comprehensible. Further analysis show a relation between the dominant features of the Best₁₀ set and the emission lines of quasars, which correspond to the peaks of importance of the different features along the redshift distribution. The same analysis done on the Classic₁₀ features proves that the latter are not able to capture the same physical information as compact as the selected features. This explains why the results obtained with the proposed method are outstanding with respect to the ones obtained with the Classic₁₀ features. Moreover, we demonstrate that the proposed features fill the redshift space in a complementary way, each adding information that is relevant in different redshift ranges. The proposed method is highly stable, as shown from the distribution of the features and the groups they belong to. The experiments show that the useful information is concentrated in a reduced number of features, which are typically very different from the Classic₁₀. Furthermore, we verified that the difference in terms of performance with respect to the various sets is almost negligible. This demonstrate that the true advantage with respect to the Classic₁₀ features is not given by the selected features themselves, but from their distribution and type in the specific set. Therefore, the stability shown from the different branches, e.g. the common distribution scheme of the features, and the ability to better capture the underlying physical processes, explains the superior performance obtained. The method is very general and could be applied to several tasks in astrophysics (and not only in astrophysics). In the future we propose to apply it to different sources (i.e. galaxies with and without an active nuclei) in order to verify if the obtained features are general or if they are only related to the fine structure of the data itself and to this specific population of sources. This includes the question how much the processes of the active galactic nuclei dominate with respect to the processes in the surrounding galaxy the feature selection approach. It goes without saying, that this first step done in the interpretation of the new features could open new doors in the understanding of the physics of quasars with respect to distance/age by providing better and more precise tracers. On the other hand, the method shows a different approach alternative to the application of deep learning, but also employing intensively GPUs. Both approaches are meant to establish an affordable and good performing method to precisely predict photometric redshifts, in prevision of the upcoming missions and instruments in the near future.

Acknowledgements. The authors gratefully acknowledge the support of the Klaus Tschira Foundation. SC acknowledges support from the project ‘‘Quasars at high redshift: physics and Cosmology’’ financed by the ASI/INAF agreement 2017-14-H.0. We would like to thank Nikos Gianniotis and Erica Hopkins for proofreading and commenting on this work. Topcat has been used for this work (Taylor 2005). The DCMND model has been developed using Theano (The Theano Development Team et al. 2016). To extract the image for the DCMND we made use of HIPS (Fernique et al. 2015) and Montage (Berriman et al. 2004). Montage is funded by the National Science Foundation under Grant Number ACI-1440620, and was previously funded by the National Aeronautics and Space Administration’s Earth Science Technology Office, Computation Technologies Project, under Cooperative Agreement Number NCC5-626 between NASA and the California Institute of Technology. Funding for the SDSS and SDSS-II has been provided by the Alfred P. Sloan Foundation, the Participating Institutions, the National Science Foundation, the U.S. Department of Energy, the National Aeronautics and Space Administration, the Japanese Mombukagakusho, the Max Planck Society, and the Higher Education Funding Council for England. The SDSS Web Site is <http://www.sdss.org/>. The SDSS is managed by the Astrophysical Research Consortium for the Participating Institutions. The Participating Institutions are the American Museum of Natural History, Astrophysical Institute Potsdam, University of Basel, University of Cambridge, Case Western Reserve University, University of Chicago, Drexel University, Fermilab, the Institute for Advanced Study, the Japan Participation Group, Johns Hopkins University, the Joint Institute for Nuclear Astrophysics, the Kavli Institute for Particle Astrophysics and Cosmology, the Korean Scientist Group, the Chinese Academy of Sciences (LAMOST), Los Alamos National

⁵ using Wright (2006) with $H_0 = 69.6$, $\Omega_M = 0.286$, $\Omega_{DE} = 0.714$

Laboratory, the Max-Planck-Institute for Astronomy (MPIA), the Max-Planck-Institute for Astrophysics (MPA), New Mexico State University, Ohio State University, University of Pittsburgh, University of Portsmouth, Princeton University, the United States Naval Observatory, and the University of Washington.

References

- Abazajian, K. N., Adelman-McCarthy, J. K., Agüeros, M. A., et al. 2009, *ApJS*, 182, 543
- Ahn, C. P., Alexandroff, R., Allende Prieto, C., et al. 2012, *ApJS*, 203, 21
- Aksoy, S. & Haralick, R. M. 2000, *Pattern Recognition Letters*, 22, 563
- Athiwaratkun, B. & Kang, K. 2015, *ArXiv e-prints* [arXiv:1507.02313]
- Ball, N. M., Brunner, R. J., Myers, A. D., et al. 2008, *ApJ*, 683, 12
- Beck, R., Lin, I., Ishida, E., et al. 2017, *Monthly Notices of the Royal Astronomical Society*, 468, 4323
- Benavente, P., Protopapas, P., & Pichara, K. 2017, *Astrophysical Journal*, 845
- Berriman, G. B., Good, J. C., Laity, A. C., et al. 2004, in *Astronomical Society of the Pacific Conference Series*, Vol. 314, *Astronomical Data Analysis Software and Systems (ADASS) XIII*, ed. F. Ochsenbein, M. G. Allen, & D. Egret, 593
- Bilicki, M., Jarrett, T. H., Peacock, J. A., Cluver, M. E., & Steward, L. 2014, *ApJS*, 210, 9
- Bishop, C. M. 2006, *Pattern Recognition and Machine Learning (Information Science and Statistics)* (Secaucus, NJ, USA: Springer-Verlag New York, Inc.)
- Bonnett, C., Troxel, M. A., Hartley, W., et al. 2016, *Phys. Rev. D*, 94, 042005
- Breiman, L. 1996, *Machine Learning*, 24, 123
- Breiman, L., Friedman, J., Olshen, R., & Stone, C. 1984, *Classification and Regression Trees* (Monterey, CA: Wadsworth and Brooks)
- Carliles, S., Budavári, T., Heinis, S., Priebe, C., & Szalay, A. S. 2010, *ApJ*, 712, 511
- Cavuoti, S., Brescia, M., D'Abrusco, R., Longo, G., & Paolillo, M. 2013a, *Monthly Notices of the Royal Astronomical Society*, 437, 968
- Cavuoti, S., Brescia, M., De Stefano, V., & Longo, G. 2015, *Experimental Astronomy*, 39, 45
- Cavuoti, S., Garofalo, M., Brescia, M., et al. 2013b, *Smart Innovation, Systems and Technologies*, 19, 29
- Chambers, K. C., Magnier, E. A., Metcalfe, N., et al. 2016, *ArXiv e-prints* [arXiv:1612.05560]
- D'Abrusco, R., Staiano, A., Longo, G., et al. 2007, *ApJ*, 663, 752
- de Jong, J. T. A., Verdoes Kleijn, G. A., Erben, T., et al. 2017, *Astronomy and Astrophysics* 604, A134 [arXiv:1703.02991]
- D'Isanto, A., Cavuoti, S., Brescia, M., et al. 2016, *Monthly Notices of the Royal Astronomical Society*, 457, 3119
- D'Isanto, A. & Polsterer, K. L. 2018, *A&A*, 609, A111
- Donalek, C., Arun Kumar, A., Djorgovski, S. G., et al. 2013, *ArXiv e-prints* [arXiv:1310.1976]
- Duda, R. O., Hart, P. E., & Stork, D. G. 2000, *Pattern Classification (2Nd Edition)* (Wiley-Interscience)
- Fernique, P., Allen, M. G., Boch, T., et al. 2015, *A&A*, 578, A114
- Fix, E. & Hodges, J. L. 1951, *US Air Force School of Aviation Medicine, Technical Report 4*, 477+
- Gieseke, F., Polsterer, K. L., Oancea, C. E., & Igel, C. 2014, in *22th European Symposium on Artificial Neural Networks, ESANN 2014*, Bruges, Belgium, April 23-25, 2014
- Gneiting, T., Raftery, A. E., Westveld, A. H., & Goldman, T. 2005, *Monthly Weather Review*, 133, 1098
- Guyon, I. & Elisseeff, A. 2003, *J. Mach. Learn. Res.*, 3, 1157
- Harnois-Déraps, J., Tröster, T., Chisari, N., et al. 2017, *Monthly Notices of the Royal Astronomical Society*, 471, 1619
- Heinermann, J., Kramer, O., Polsterer, K., & Gieseke, F. 2013, in *KI*, Vol. 8077
- Hersbach, H. 2000, *Weather and Forecasting*, 15, 559
- Hey, T., Tansley, S., & Tolle, K., eds. 2009, *The Fourth Paradigm: Data-Intensive Scientific Discovery* (Redmond, Washington: Microsoft Research)
- Hildebrandt, H., Arnouts, S., Capak, P., et al. 2010, *Astronomy and Astrophysics*, 523, cited By 105
- Hildebrandt, H., Viola, M., Heymans, C., et al. 2016, *Monthly Notices of the Royal Astronomical Society*, 465, 1
- Hildebrandt, H., Wolf, C., & Benítez, N. 2008, *A&A*, 480, 703
- Hoyle, B. 2016, *Astronomy and Computing*, 16, 34
- Hoyle, B., Rau, M. M., Zitlau, R., Seitz, S., & Weller, J. 2015, *MNRAS*, 449, 1275
- Ivezić, v., Tyson, J. A., Acosta, E., et al. 2008, *ArXiv e-prints* [arXiv:0805.2366v4]
- Joudaki, S., Mead, A., Blake, C., et al. 2017, *Monthly Notices of the Royal Astronomical Society*, 471, 1259
- Kohavi, R. 1995, in *Proceedings of the 14th International Joint Conference on Artificial Intelligence - Volume 2, IJCAI'95* (San Francisco, CA, USA: Morgan Kaufmann Publishers Inc.), 1137–1143
- Krzywinski, M. I., Schein, J. E., Birol, I., et al. 2009, *Genome Research* [e-print]
- Köhlinger, F., Viola, M., Joachimi, B., et al. 2017, *Monthly Notices of the Royal Astronomical Society*, 471, 4412
- Laureijs, R., Amiaux, J., Arduini, S., et al. 2011, *ArXiv e-prints* [arXiv:1110.3193]
- Laurino, O., D'Abrusco, R., Longo, G., & Riccio, G. 2011, *MNRAS*, 418, 2165
- Mahabal, A., Djorgovski, S. G., Turmon, M., et al. 2008, *Astronomische Nachrichten*, 329, 288
- Mao, K. 2004, *IEEE Transactions on Systems, Man, and Cybernetics, Part B: Cybernetics*, 34, 629, cited By 68
- Norris, R. P., Hopkins, A. M., Afonso, J., et al. 2011, *PASA*, 28, 215
- Polsterer, K., Gieseke, F., & Igel, C. 2015, *Automatic galaxy classification via machine learning techniques: Parallelized rotation/flipping INvariant Kohonen maps (PINK)*, Vol. 24 (*Astronomical Society of the Pacific*), 81–86
- Polsterer, K. L., Gieseke, F., Igel, C., & Goto, T. 2014, in *Astronomical Society of the Pacific Conference Series*, Vol. 485, *Astronomical Data Analysis Software and Systems XXIII*, ed. N. Manset & P. Forshay, 425
- Richards, G. T., Myers, A. D., Gray, A. G., et al. 2009, *ApJS*, 180, 67
- Richards, G. T., Weinstein, M. A., Schneider, D. P., et al. 2001, *AJ*, 122, 1151
- Rimoldini, L., Dubath, P., Süveges, M., et al. 2012, *MNRAS*, 427, 2917
- Smirnov, E. & Markov, A. 2017, *Monthly Notices of the Royal Astronomical Society*, 469, 2024
- Tangaro, S., Amoroso, N., Brescia, M., et al. 2015, *Computational and Mathematical Methods in Medicine*, 2015
- Taylor, A. R. 2008, in *IAU Symposium*, Vol. 248, *A Giant Step: from Milli- to Micro-arcsecond Astrometry*, ed. W. J. Jin, I. Platais, & M. A. C. Perryman, 164–169
- Taylor, M. B. 2005, in *Astronomical Society of the Pacific Conference Series*, Vol. 347, *Astronomical Data Analysis Software and Systems XIV*, ed. P. Shopbell, M. Britton, & R. Ebert, 29
- The Theano Development Team, Al-Rfou, R., Alain, G., et al. 2016, *ArXiv e-prints* [arXiv:1605.02688]
- Tortora, C., La Barbera, F., Napolitano, N., et al. 2016, *Monthly Notices of the Royal Astronomical Society*, 457, 2845
- Vaccari, M., Covone, G., Radovich, M., et al. 2016, in *Proceedings of the 4th Annual Conference on High Energy Astrophysics in Southern Africa (HEASA 2016)*, January 13th, 2016, *South African Astronomical Observatory (SAAO)*, Cape Town, South Africa. Online at <http://pos.sissa.it/cgi-bin/reader/conf.cgi?confid=275>, id.26, 26
- van Haarlem, M. P., Wise, M. W., Gunst, A. W., et al. 2013, *A&A*, 556, A2
- Wright, E. L. 2006, *PASP*, 118, 1711
- Zhang, Y., Ma, H., Peng, N., Zhao, Y., & Wu, X.-b. 2013, *AJ*, 146, 22

Appendix A: Additional tables and figures

In this section, the additional tables for the features selection and the tree structure, together with the related chord diagrams, for the experiments DR7a and DR7b, are given. Hereby, a brief explanation of how to read a chord diagram follows.

Appendix A.1: Chord diagram: how to read

The chord diagram is a tool to visualize complex structures and relations in multidimensional data which is arranged in a matrix shape. The data are disposed in a circle and each element, in our case the features, is associated with a different color. The relations between the elements are expressed by ribbons which connect them, with a specific width related to the importance of that specific connection. Therefore, the different ribbons can enter or exit from every arc, representing the features. The chord diagrams utilized for this work are characterized by three external arcs for each feature. Ordered from outside to inside, the external arcs represent the occurrences of a particular feature: the total percentage of the individual connections, the numbers and sources of connections entering, and the numbers and targets of connections exiting. Therefore, starting from the first features indicated in the captions, it is possible to follow all the possible paths of the tree, depicting the different feature subsets and their global scheme. Splitting points, joints and complex interplay between feature groups can thereby be analyzed intuitively.

Appendix B: Data

The SDSS object IDs and coordinates of the extracted quasars for the three catalogs are available as supplementary information, as ASCII files.

dr7a.csv contains the SDSS object IDs and coordinates of the quasars for experiment DR7a.

dr7b.csv contains the SDSS object IDs and coordinates of the quasars for experiment DR7b.

dr7+9.csv contains the SDSS object IDs and coordinates of the quasars for experiment DR7+9.

Appendix C: Code

The code of the DCMDN model is available on the ASCL⁶

⁶ <http://www.ascl.net/ascl:1709.006>

| id | Feature 1 | Feature 2 | Feature 3 | Feature 4 | Feature 5 | Feature 6 | Feature 7 | Feature 8 | Feature 9 | Feature 10 |
|-----|-----------------------------------|-----------------------------------|-----------------------------------|-----------------------------------|-----------------------------------|-------------------------------------|-------------------------------------|--|--|-------------------------------------|
| 1 | | | | | | | | σ_{model} | $z_{\text{model}}/z_{\text{psf}}$ | $i_{\text{psf}} - i_{\text{dev}}$ |
| 2 | | | | | $g_{\text{psf}}/i_{\text{exp}}$ | $i_{\text{psf}}/z_{\text{model}}$ | | $z_{\text{model}}/z_{\text{psf}}$ | σ_{model} | |
| 3 | | | | | | | | | | $g_{\text{petro}}/r_{\text{petro}}$ |
| 4 | | | | $r_{\text{psf}}/i_{\text{model}}$ | | | | σ_{model} | $z_{\text{model}}/z_{\text{psf}}$ | $i_{\text{dev}}/i_{\text{psf}}$ |
| 5 | | | | | | | $i_{\text{psf}} - i_{\text{petro}}$ | | | |
| 6 | | | | | $i_{\text{psf}}/z_{\text{model}}$ | $g_{\text{petro}}/r_{\text{petro}}$ | | σ_{model} | | $i_{\text{psf}} - i_{\text{dev}}$ |
| 7 | | | | | | | | $z_{\text{model}}/z_{\text{psf}}$ | $\sqrt{\sigma_{\text{model}}^2 + \sigma_{\text{dev}}^2}$ | |
| 8 | $i_{\text{psf}}/i_{\text{exp}}$ | | $r_{\text{psf}}/i_{\text{exp}}$ | | | | | | | $i_{\text{dev}}/i_{\text{psf}}$ |
| 9 | | | | | | | | $i_{\text{dev}}/i_{\text{psf}}$ | σ_{model} | |
| 10 | | | | | $g_{\text{psf}}/i_{\text{exp}}$ | $i_{\text{psf}}/z_{\text{model}}$ | $i_{\text{dev}}/i_{\text{psf}}$ | σ_{model} | $r_{\text{psf}} - r_{\text{petro}}$ | $g_{\text{petro}}/r_{\text{petro}}$ |
| 11 | | $g_{\text{psf}}/i_{\text{model}}$ | | | | | | $\sqrt{\sigma_{\text{model}}^2 + \sigma_{\text{dev}}^2}$ | | |
| 12 | | | | $z_{\text{model}}/z_{\text{psf}}$ | | | | σ_{model} | $z_{\text{model}}/z_{\text{psf}}$ | $i_{\text{psf}} - i_{\text{dev}}$ |
| 13 | | | | | | | | σ_{model} | σ_{model} | $r_{\text{psf}} - r_{\text{petro}}$ |
| 14 | | | | | | | $i_{\text{psf}} - i_{\text{petro}}$ | $i_{\text{dev}}/i_{\text{psf}}$ | | $r_{\text{dev}}/r_{\text{psf}}$ |
| 15 | | | | | $i_{\text{psf}}/z_{\text{model}}$ | $g_{\text{petro}}/r_{\text{petro}}$ | | | $\sqrt{\sigma_{\text{model}}^2 + \sigma_{\text{dev}}^2}$ | $r_{\text{psf}} - r_{\text{petro}}$ |
| 16 | | | | | | | | | | $r_{\text{dev}}/r_{\text{psf}}$ |
| 17 | | | | | | | | σ_{model} | | |
| 18 | | | | | | | | $\sqrt{\sigma_{\text{model}}^2 + \sigma_{\text{dev}}^2}$ | $z_{\text{model}}/z_{\text{psf}}$ | $i_{\text{psf}} - i_{\text{petro}}$ |
| 19 | $i_{\text{psf}}/i_{\text{model}}$ | | $r_{\text{psf}}/i_{\text{model}}$ | $i_{\text{dev}}/i_{\text{psf}}$ | $r_{\text{psf}}/g_{\text{model}}$ | | $r_{\text{psf}} - r_{\text{petro}}$ | | | |
| 20* | | | | | | | | $\sqrt{\sigma_{\text{model}}^2 + \sigma_{\text{dev}}^2}$ | | |
| 21 | | | | | $g_{\text{psf}}/i_{\text{exp}}$ | | | σ_{model} | $g_{\text{petro}}/r_{\text{petro}}$ | $z_{\text{model}}/z_{\text{psf}}$ |
| 22 | | | | | | | | | | $i_{\text{psf}} - i_{\text{petro}}$ |

Table C.1. Detailed feature branches obtained from the feature selection for the experiment DR7a. The 20th branch, indicated with the * symbol, is the best performing subset with respect to the experiments using the RF. The *ratios* and *photometric ratios* are indicated, respectively, with vertical lines and dots. The *differences* are marked with horizontal lines and the *errors* with north west lines. The color code for the features is the same as shown in the chord diagram in Fig. C.1.

Experiment DR7a

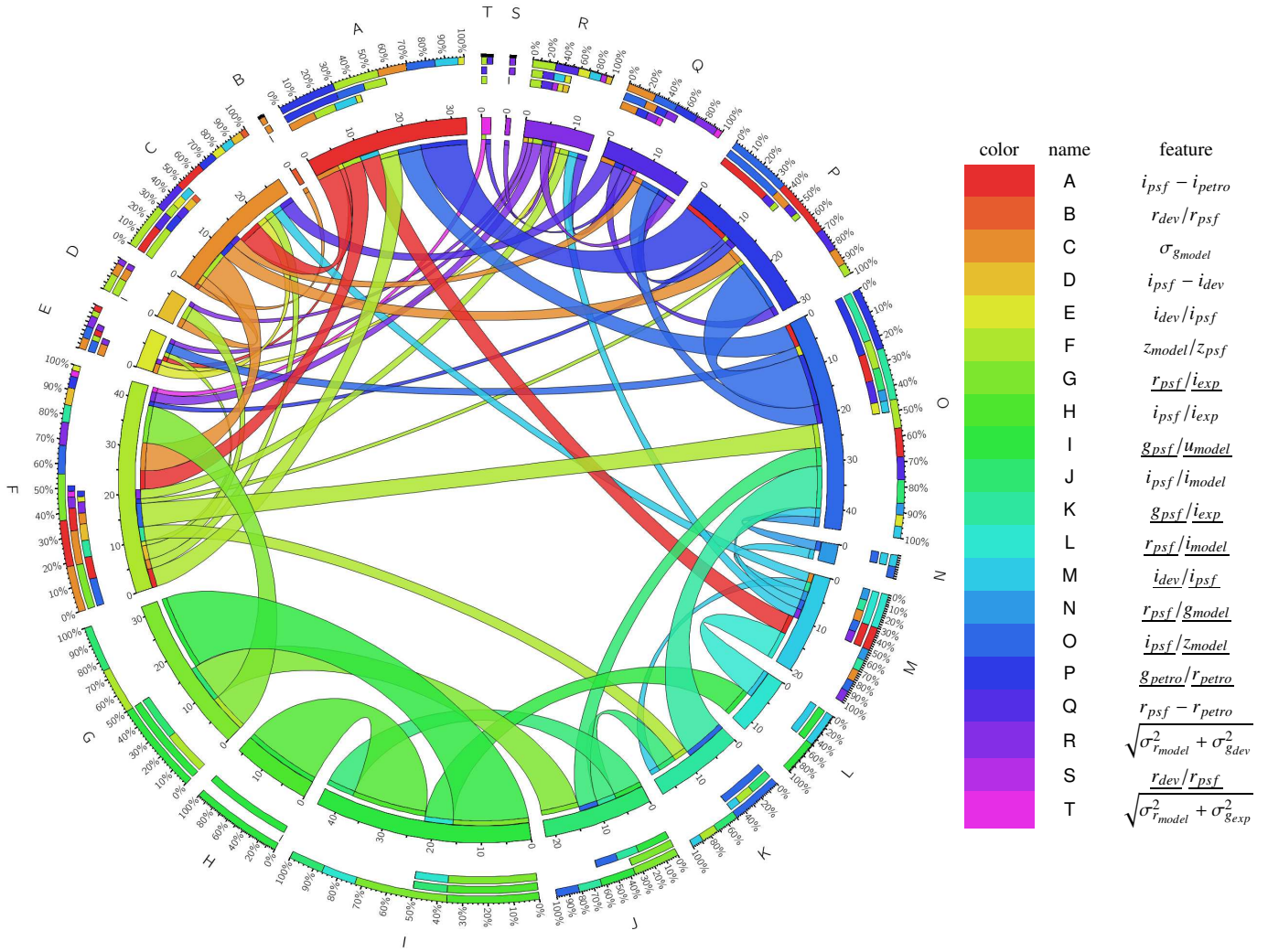


Fig. C.1. Chord diagram for the experiment DR7a. Every feature is associated to a specific color, and starting from the first features (H,J) it is possible to follow all the possible paths of the tree, depicting the different feature subsets.

| id | Feature 1 | Feature 2 | Feature 3 | Feature 4 | Feature 5 | Feature 6 | Feature 7 | Feature 8 | Feature 9 | Feature 10 |
|-----|---------------------|-----------------------------|-----------------------------|-----------------------|---------------------|-----------------------------|-----------------------|-----------------------|--|--|
| 1 | | | | | | | | $r_{psf} - r_{petro}$ | $i_{psf} - i_{dev}$ | |
| 2 | | | | | | $\frac{R_{psf}}{r_{model}}$ | | | i_{dev}/i_{psf} | |
| 3 | | | | | | | | $i_{psf} - i_{dev}$ | $r_{psf} - r_{petro}$ | $\sqrt{\sigma_{model}^2 + \sigma_{dev}^2}$ |
| 4 | | | | | | | | | $i_{psf} - i_{dev}$ | |
| 5 | | | | | i_{psf}/z_{model} | | | $r_{psf} - r_{petro}$ | i_{dev}/i_{psf} | |
| 6 | | | | | | $\frac{R_{psf}}{r_{exp}}$ | | | | $\delta_{psf} - \delta_{dev}$ |
| 7 | | | | | | | | $i_{psf} - i_{dev}$ | | $\sqrt{\sigma_{model}^2 + \sigma_{dev}^2}$ |
| 8 | | | | | | | | i_{dev}/i_{psf} | | |
| 9 | i_{psf}/i_{exp} | | $\frac{r_{psf}}{i_{exp}}$ | z_{model}/z_{psf} | | | | $i_{psf} - i_{petro}$ | | $\delta_{psf} - \delta_{dev}$ |
| 10 | | | | | | | | $i_{psf} - i_{dev}$ | | $\sqrt{\sigma_{model}^2 + \sigma_{dev}^2}$ |
| 11 | | | | | | $\frac{R_{psf}}{r_{model}}$ | | | | $r_{petroR} - z_{petroR90}$ |
| 12 | | | | | | | | i_{dev}/i_{psf} | $r_{psf} - r_{petro}$ | $\sqrt{\sigma_{model}^2 + \sigma_{dev}^2}$ |
| 13* | | | | | z_{psf}/i_{model} | | | | | $\delta_{psf} - \delta_{dev}$ |
| 14 | | | | | | | | $i_{psf} - i_{dev}$ | | $\sqrt{\sigma_{model}^2 + \sigma_{dev}^2}$ |
| 15 | | | | | | $\frac{R_{psf}}{r_{exp}}$ | | | | $\delta_{psf} - \delta_{dev}$ |
| 16 | | | | | | | | | | $\sqrt{\sigma_{model}^2 + \sigma_{dev}^2}$ |
| 17 | | | | | | | | | | $\delta_{psf} - \delta_{dev}$ |
| 18 | | | | | | | | | | z_{exp}/z_{psf} |
| 19 | | | | | | | i_{dev}/r_{psf} | i_{dev}/i_{psf} | $\sqrt{\sigma_{model}^2 + \sigma_{dev}^2}$ | z_{model}/z_{psf} |
| 20 | | $\frac{R_{psf}}{i_{model}}$ | | | i_{psf}/z_{model} | $\frac{R_{psf}}{r_{model}}$ | | | | $\delta_{psf} - \delta_{dev}$ |
| 21 | | | | | | | z_{model}/z_{psf} | | $r_{psf} - r_{petro}$ | $\sqrt{\sigma_{model}^2 + \sigma_{dev}^2}$ |
| 22 | | | | $i_{psf} - i_{petro}$ | | | | | | $\delta_{psf} - \delta_{dev}$ |
| 23 | | | | | | $\frac{R_{psf}}{r_{petro}}$ | | $r_{psf} - r_{petro}$ | | $\sqrt{\sigma_{model}^2 + \sigma_{dev}^2}$ |
| 24 | | | | | | | | $r_{psf} - r_{petro}$ | z_{model}/z_{psf} | |
| 25 | | | | | | | i_{dev}/i_{psf} | | | $r_{petroR} - z_{petroR90}$ |
| 26 | | | | | | $\frac{r_{psf}}{R_{exp}}$ | r_{psf}/r_{psf} | r_{psf}/r_{psf} | $\sqrt{\sigma_{model}^2 + \sigma_{dev}^2}$ | z_{model}/z_{psf} |
| 27 | | | | | z_{psf}/i_{exp} | | i_{dev}/r_{psf} | i_{dev}/i_{psf} | | |
| 28 | | | | | | | | | | $r_{petroR} - z_{petroR90}$ |
| 29 | i_{psf}/i_{model} | | $\frac{r_{psf}}{i_{model}}$ | | | | | | | i_{psf}/z_{petro} |
| 30 | | | | | | $\frac{r_{psf}}{R_{petro}}$ | | | | $\sqrt{\sigma_{model}^2 + \sigma_{dev}^2}$ |
| 31 | | | | | | | | | | i_{psf}/z_{petro} |
| 32 | | | | | | $\frac{r_{psf}}{R_{exp}}$ | | | | $\sqrt{\sigma_{model}^2 + \sigma_{dev}^2}$ |
| 33 | | | | | i_{psf}/z_{model} | $\frac{R_{psf}}{r_{model}}$ | | | | |
| 34 | | | | i_{dev}/i_{psf} | | | $r_{psf} - r_{petro}$ | $i_{psf} - i_{petro}$ | z_{model}/z_{psf} | $\delta_{psf} - \delta_{dev}$ |
| 35 | | | | | | | | | | $\sqrt{\sigma_{model}^2 + \sigma_{dev}^2}$ |
| 36 | | | | | | $\frac{r_{psf}}{R_{exp}}$ | | | | |
| 37 | | | | | | | | | | i_{psf}/z_{petro} |
| 38 | | | | | z_{psf}/i_{model} | | | | | $r_{petroR} - z_{petroR90}$ |
| 39 | | | | | | | | | | $\sqrt{\sigma_{model}^2 + \sigma_{dev}^2}$ |
| 40 | | | | | | $\frac{r_{psf}}{R_{model}}$ | | | | $r_{petroR} - z_{petroR90}$ |
| 41 | | | | | | | | | | $\delta_{model} - \delta_{exp}$ |

Table C.2. Detailed feature branches obtained from the feature selection for the experiment DR7b. The 13th branch, indicated with the * symbol, is the best performing subset with respect to the experiments using the RF. The *ratios* and *photometric ratios* are indicated, respectively, with vertical lines and dots. The *differences* are marked with horizontal lines and the *errors* are with north west lines. Finally, the only feature composed by radius is indicated with a grid. The color code for the features is the as same shown in the chord diagram in Fig. C.2

Experiment DR7b

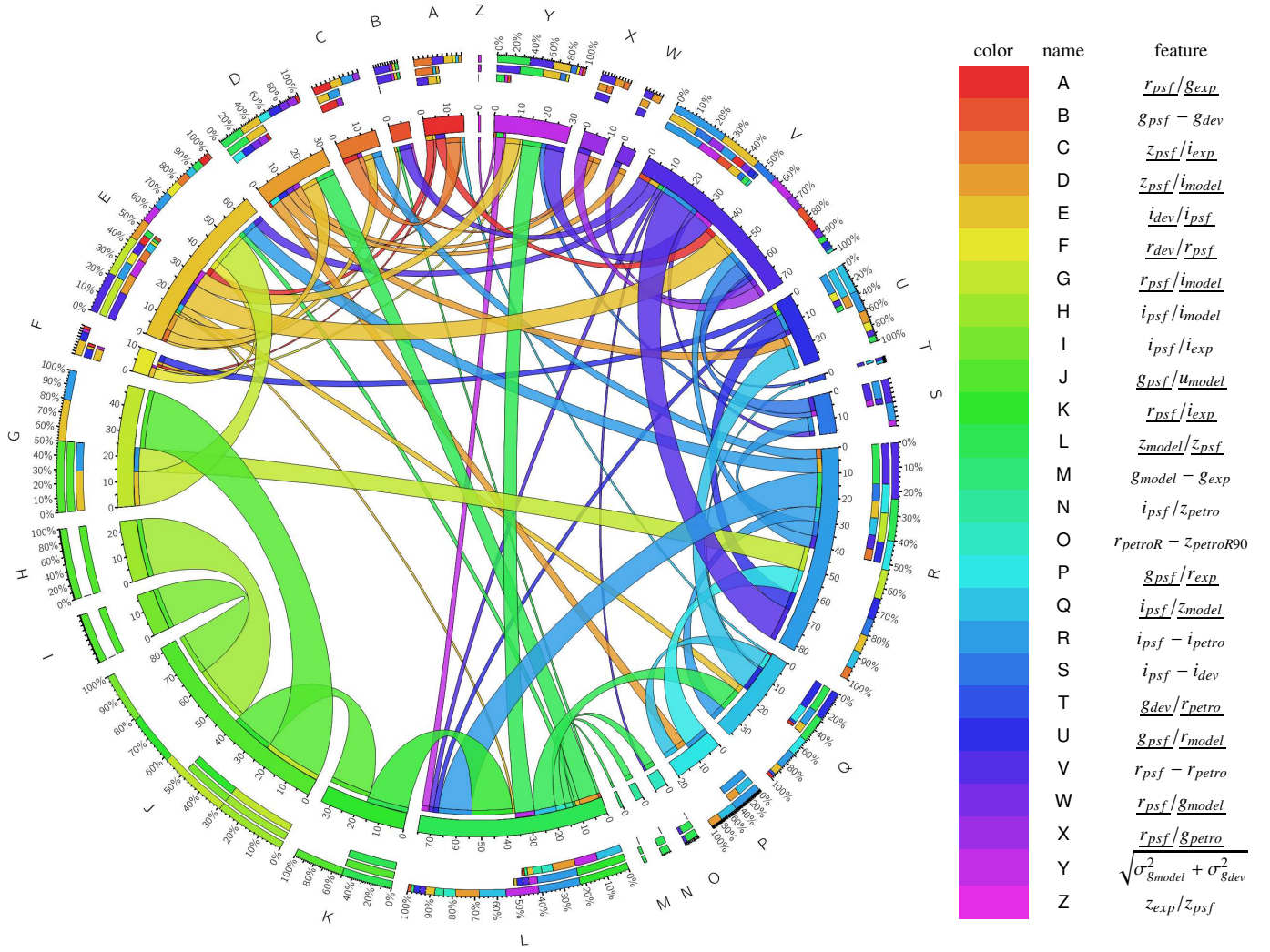


Fig. C.2. Chord diagram for the experiment DR7b. Every feature is associated to a specific color, and starting from the first features (H,I) it is possible to follow all the possible paths of the tree, depicting the different feature subsets.

Appendix D: SDSS QSO query

In the following, the statements used to query the SDSS database are provided.

Appendix D.1: Experiment DR7

```
SELECT
  s.specObjID, p.objid, p.ra, p.dec, s.targetObjID, s.z, s.zErr,
  p.psfMag_u, p.psfMag_g, p.psfMag_r, p.psfMag_i, p.psfMag_z,
  p.psfMagErr_u, p.psfMagErr_g, p.psfMagErr_r, p.psfMagErr_i, p.psfMagErr_z,
  p.modelMag_u, p.modelMag_g, p.modelMag_r, p.modelMag_i, p.modelMag_z,
  p.modelMagErr_u, p.modelMagErr_g, p.modelMagErr_r, p.modelMagErr_i, p.modelMagErr_z,
  p.devMag_u, p.devMag_g, p.devMag_r, p.devMag_i, p.devMag_z,
  p.devMagErr_u, p.devMagErr_g, p.devMagErr_r, p.devMagErr_i, p.devMagErr_z,
  p.expMag_u, p.expMag_g, p.expMag_r, p.expMag_i, p.expMag_z,
  p.expMagErr_u, p.expMagErr_g, p.expMagErr_r, p.expMagErr_i, p.expMagErr_z,
  p.petroMag_u, p.petroMag_g, p.petroMag_r, p.petroMag_i, p.petroMag_z,
  p.petroMagErr_u, p.petroMagErr_g, p.petroMagErr_r, p.petroMagErr_i, p.petroMagErr_z,
  p.extinction_u, p.extinction_g, p.extinction_r, p.extinction_i, p.extinction_z,
  p.devRad_u, p.devRad_g, p.devRad_r, p.devRad_i, p.devRad_z,
  p.expRad_u, p.expRad_g, p.expRad_r, p.expRad_i, p.expRad_z,
  p.petroRad_u, p.petroRad_g, p.petroRad_r, p.petroRad_i, p.petroRad_z,
  p.petroR90_u, p.petroR90_g, p.petroR90_r, p.petroR90_i, p.petroR90_z,
  p.petroR50_u, p.petroR50_g, p.petroR50_r, p.petroR50_i, p.petroR50_z,
  p.devAB_u, p.devAB_g, p.devAB_r, p.devAB_i, p.devAB_z,
  p.expAB_u, p.expAB_g, p.expAB_r, p.expAB_i, p.expAB_z
```

FROM

SpecPhoto as s, PhotoObjAll as p

WHERE

```
p.mode = 1 AND p.SpecObjID = s.SpecObjID AND
dbo.fPhotoFlags('PEAKCENTER') != 0 AND
dbo.fPhotoFlags('NOTCHECKED') != 0 AND
dbo.fPhotoFlags('DEBLEND_NOPEAK') != 0 AND
dbo.fPhotoFlags('PSF_FLUX_INTERP') != 0 AND
dbo.fPhotoFlags('BAD_COUNTS_ERROR') != 0 AND
dbo.fPhotoFlags('INTERP_CENTER') != 0 AND
p.objid=s.objid and (specClass = 3 OR specClass = 4) AND
s.psfMag_i > 14.5 AND (s.psfMag_i - s.extinction_i) < 21.3 AND
s.psfMagErr_i < 0.2
```

Appendix D.2: Experiment DR7b

SELECT

```
s.specObjID, p.objid, p.ra, p.dec, s.targetObjID, s.z, s.zErr,
p.psfMag_u, p.psfMag_g, p.psfMag_r, p.psfMag_i, p.psfMag_z,
p.psfMagErr_u, p.psfMagErr_g, p.psfMagErr_r, p.psfMagErr_i, p.psfMagErr_z,
p.modelMag_u, p.modelMag_g, p.modelMag_r, p.modelMag_i, p.modelMag_z,
p.modelMagErr_u, p.modelMagErr_g, p.modelMagErr_r, p.modelMagErr_i, p.modelMagErr_z,
p.devMag_u, p.devMag_g, p.devMag_r, p.devMag_i, p.devMag_z,
p.devMagErr_u, p.devMagErr_g, p.devMagErr_r, p.devMagErr_i, p.devMagErr_z,
p.expMag_u, p.expMag_g, p.expMag_r, p.expMag_i, p.expMag_z,
p.expMagErr_u, p.expMagErr_g, p.expMagErr_r, p.expMagErr_i, p.expMagErr_z,
p.petroMag_u, p.petroMag_g, p.petroMag_r, p.petroMag_i, p.petroMag_z,
p.petroMagErr_u, p.petroMagErr_g, p.petroMagErr_r, p.petroMagErr_i, p.petroMagErr_z,
p.extinction_u, p.extinction_g, p.extinction_r, p.extinction_i, p.extinction_z,
p.devRad_u, p.devRad_g, p.devRad_r, p.devRad_i, p.devRad_z,
p.expRad_u, p.expRad_g, p.expRad_r, p.expRad_i, p.expRad_z,
p.petroRad_u, p.petroRad_g, p.petroRad_r, p.petroRad_i, p.petroRad_z,
p.petroR90_u, p.petroR90_g, p.petroR90_r, p.petroR90_i, p.petroR90_z,
p.petroR50_u, p.petroR50_g, p.petroR50_r, p.petroR50_i, p.petroR50_z,
p.devAB_u, p.devAB_g, p.devAB_r, p.devAB_i, p.devAB_z,
p.expAB_u, p.expAB_g, p.expAB_r, p.expAB_i, p.expAB_z
```

```
into mydb.qso_dr7_noflags from SpecPhoto as s, PhotoObjAll as p
```

```
WHERE
```

```
p.SpecObjID = s.SpecObjID AND
p.objid=s.objid and (specClass = 3 OR specClass = 4)
```

Appendix D.3: Experiment DR7+9

```
SELECT
```

```
m.objid, m.ra AS ra1, m.dec AS dec1,
n.objid, n.distance,
p.ra AS ra2, p.dec AS dec2,
p.objid, p.ra, p.dec, p.psfMag_u, p.psfMag_g, p.psfMag_r, p.psfMag_i,
p.psfMag_z, p.psfMagErr_u, p.psfMagErr_g, p.psfMagErr_r, p.psfMagErr_i,
p.psfMagErr_z, p.modelMag_u, p.modelMag_g, p.modelMag_r, p.modelMag_i, p.modelMag_z,
p.modelMagErr_u, p.modelMagErr_g, p.modelMagErr_r, p.modelMagErr_i,
p.modelMagErr_z, p.devMag_u, p.devMag_g, p.devMag_r, p.devMag_i, p.devMag_z,
p.devMagErr_u, p.devMagErr_g, p.devMagErr_r, p.devMagErr_i, p.devMagErr_z,
p.expMag_u, p.expMag_g, p.expMag_r, p.expMag_i, p.expMag_z, p.expMagErr_u, p.expMagErr_g,
p.expMagErr_r, p.expMagErr_i, p.expMagErr_z, p.petroMag_u, p.petroMag_g, p.petroMag_r,
p.petroMag_i, p.petroMag_z, p.petroMagErr_u, p.petroMagErr_g, p.petroMagErr_r,
p.petroMagErr_i, p.petroMagErr_z, p.extinction_u, p.extinction_g, p.extinction_r,
p.extinction_i, p.extinction_z, p.devRad_u, p.devRad_g, p.devRad_r, p.devRad_i,
p.devRad_z, p.expRad_u, p.expRad_g, p.expRad_r, p.expRad_i, p.expRad_z, p.petroRad_u,
p.petroRad_g, p.petroRad_r, p.petroRad_i, p.petroRad_z, p.petroR90_u, p.petroR90_g,
p.petroR90_r, p.petroR90_i, p.petroR90_z, p.petroR50_u, p.petroR50_g, p.petroR50_r,
p.petroR50_i, p.petroR50_z, p.devAB_u, p.devAB_g, p.devAB_r, p.devAB_i, p.devAB_z, p.expAB_u,
p.expAB_g, p.expAB_r, p.expAB_i, p.expAB_z
into mydb.quasar_dr7_dr9_allphoto from MyDB.dr7_dr9_quasar AS m
```

```
CROSS APPLY dbo.fGetNearestObjEq( m.ra, m.dec, 0.5) AS n
JOIN PhotoObj AS p ON n.objid=p.objid
```